Chapter 6

RF system

6.1 RF System Overview

RF-related machine parameters for SuperKEKB main rings (LER and HER) are shown in Table 6.1. The beam currents in both rings of SuperKEKB (3.6 A and 2.6 A) are approximately double those achieved in KEKB (2.0 A and 1.4 A). The most serious issue we have to address to store these large beam currents is the excitation of fast-growing longitudinal coupled-bunch instabilities (CBI) caused by the accelerating mode of detuned RF cavities which is needed to compensate for the reactive component of beam-loading. The cavity higher-order mode (HOM) impedances also have to be minimized not to drive strong longitudinal and transverse CBI as well as to reduce the induced HOM power. Another issue is the transient beam loading due to bunch gaps, because it causes relative phase difference of colliding beams bunch-by-bunch, which results in luminosity degradation and may deteriorate beam stability in the worst case.

To overcome these difficulties, two types of innovative heavily HOM-damped cavities, normal conducting cavities of the three-cavity system named ARES and single-cell superconducting cavities (SCC), were used in KEKB. An increase in the stored energy in these cavities reduces the growth rate of the CBI and also mitigates the gap transient effects. Since the ARES has a larger stored energy, this alone was used for the LER that stored the higher beam current. The HER, where a higher RF voltage was required, was equipped with a combination of the SCC and ARES. They were operated with a suitable relative phase angle to assign higher cavity voltage to the SCC and heavier beam loading to the ARES. The layout of the KEKB RF system is shown in Fig. 6.1 (top). A set of typical RF-related parameters for the physics run is also shown.

Paramter	LER	HER
Beam Energy [GeV]	4.0	7.0
Beam current [A]	3.6	2.6
Bunch gap length [%]	2	2
Bunch length [mm] (rms)	6	5
RF frequency [MHz]	508.876	
Harmonic number	5120	
Revolution frequency [kHz]	99.4	
Cavity type	ARES	SCC/ARES
Number of cavities	22	8/8
Total RF voltage [MV]	10∼11	15∼16
RF voltage/cavity [MV]	0.5	1.5/0.5
Wall loss/cavity [kW]	150	-/150
Number of klystrons	18	8/8
Klystrons power [kW]	∼600	∼450/∼800
Beam power [MW]	∼8	∼8.3

Table 6.1: RF-related machine parameters.

Each RF station consists of a klystron, the high-power RF (HPRF) and low-level RF control (LLRF) systems, and either the ARES or SCC. The HPRF and LLRF systems are accommodated in the RF buildings, and the ARES and SCC are located in the tunnel.

The KEKB RF system with the ARES and SCC showed excellent performance during the physics run operation of KEKB. The LER beam current for the physics run was limited up to about 1.8 A, which is lower than the design current of 2.6 A, due to beam blow-up caused by the electron cloud effect. In order to check the performance of the RF system with a higher beam current, the beam current was increased up to 2.0 A at an accelerator study with a bunch spacing of three buckets. The RF system worked at this current without any problems. In order to increase the luminosity with the limited LER beam current, the HER beam current was increased beyond the design current of 1.1 A. The power delivered to the beam by each SC cavity was increased from the design value of 250 kW to 350 kW (one cavity was operated at about 400 kW), and the HER beam current was successfully increased up to 1.4 A. The HOM damping property of the ARES and the SCC was sufficient for the KEKB beam currents, and no CBI caused by the cavity HOMs was observed throughout the operation. The frequency of beam aborts caused by any kind of RF trips at all ARES or SCC stations

was typically only once per day. For details of the KEKB RF system, refer to [1, 2].

The SuperKEKB RF system design was investigated in the context of possibility of using the existing RF system for KEKB with the ARES and SCC as much as possible, by introducing necessary improvements and reinforcements. In particular, following points are important, which all are related to the much higher beam currents compared to those in KEKB.

- The RF system should deliver power to the stored beam up to approximately $\sim$8 MW per ring, which is about double that in KEKB.
- Availability of present HOM dampers should be evaluated at the SuperKEKB design parameters, and necessary measures need to be investigated.
- Beam-loading related issues and measures should be investigated: in particular the CBI associated with the accelerating mode of cavities, gap transient effects, stability and accuracy of the control performance with heavy beam-loading.

First, the twice beam current together with a larger radiation loss per turn in the LER increases the beam power more than double that of KEKB. The beam power in the HER also increases due to the higher beam current. On the other hand, the required RF voltage is about the same as that of KEKB. Consequently, each cavity should provide much higher power to the beam than the case of KEKB. To meet the requirement, the RF stations with the ARES cavities need to be changed from the KEKB scheme, where one klystron drives two cavities, to a new scheme where one klystron drives one cavity. To change to the new scheme, reinforcement of the RF source, including klystrons and other HPRF components, the LLRF system, as well as rearrangement of ARES cavities are required. The RF parameters are chosen with the klystron output power up to 850 kW in operation regardless of the maximum rated output power of 1.2 MW for the existing Toshiba tubes. This choice has advantages: (1) the existing power supplies for the klystrons can be used without major modifications, (2) most of the existing high power RF components can also be reused, and (3) the klystrons are operated below saturation with a sufficient margin, which benefits stable control under heavy beam-loading. In consideration of such terms and conditions, the RF system configuration and design parameters at its ultimate stage to store the design beam currents were optimized as shown in Table 6.1 and Fig. 6.1 (bottom).

In order to increase the power delivered to beam by each ARES cavity, the input couplers are needed to be replaced with new ones that have a stronger input coupling factor of $\beta = 6.0$ ($\beta = 2.7$ for KEKB). The new input couplers are developed, and high-power performance with beam was demonstrated at the end of the KEKB operation

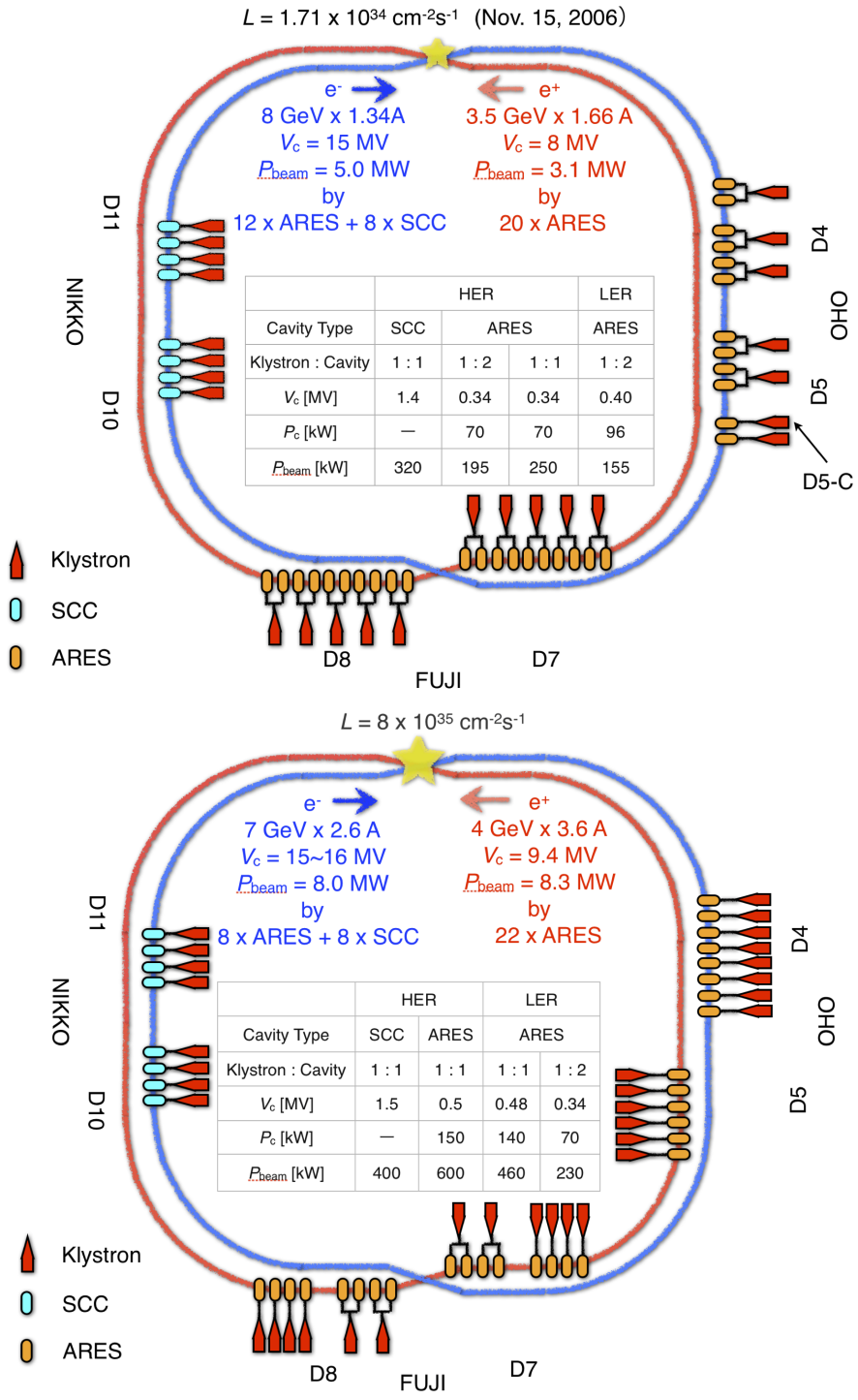

Figure 6.1: The layout of RF system, together with typical RF-related machine parameters. (top): The KEKB RF system with parameters (as of Nov. 15, 2006) for physics run. (bottom): The SuperKEKB RF system at its ultimate stage to achieve the design luminosity of $8 \times 10^{35}\ cm^{-2}s^{-1}$, together with parameters listed as an example.

in 2010. Two stations (D5-C and D5-E) were changed to the new scheme where one klystron drives one cavity, and a prototype input coupler with a higher input coupling factor was attached to the D5-C cavity. By changing the phase of this station relative to all other stations, beam loading to this station was increased. Finally, the beam power provided by the cavity reached 610kW, which meets the requirement for SuperKEKB. Following the success of the demonstration in beam operation, mass production of the new input couplers started and is ongoing, as described in Section 6.2.6.

Second, the higher beam currents together with a shorter bunch length compared to KEKB will increase the HOM power induced in the cavity region. Careful investigations were conducted to check whether the present HOM dampers are usable or not at the design beam currents of SuperKEKB. Based on the evaluation of HOM power at the ARES and related bench tests of the HOM dampers, it has been concluded that the present HOM dampers for the ARES cavities can be used without any modification, as described in detail in Section 6.2.5. On the other hand, the capacity of the existing HOM dampers for the SCC is not sufficient for the design beam current of the HER. Several measures to reduce the HOM power or to improve the HOM damper with its cooling system have been investigated. It was found that implementing an additional damper made of SiC between the adjacent SCC reduces HOM power absorbed by the existing HOM dampers made of ferrite, as described in Section 6.3.2. This measure is considered to have a lower risk and in lower cost compared to the other measures such as replacing the existing dampers with some new ones or changing configuration of beam pipes and tapers around the SCC to reduce the loss factor. Consequently, an additional SiC damper will be implemented in one of the SCC before the phase 1 commissioning. After proving the performance with the beam, this measure will be expanded to the other SCCs.

Third, the LLRF system is reexamined by taking higher beam currents into consideration. While the existing analog-based LLRF system, which had been operated stably for KEKB, can also be used for SuperKEKB, a new digital LLRF system is being developed for higher accuracy and flexibility. The new digital LLRF systems utilizes EPICS embedded FPGA board in the micro-TCA platform and also EPICS embedded PLC. A prototype one has been tested successfully with an ARES cavity to verify the performance in high-power operation. After the successful test, mass production of new digital LLRF started. Nine existing LLRF systems located at the Oho building, which suffered serious damage from the Great East Japan Earthquake, are being replaced with the new LLRF system. Since compatibility between the existing and new LLRF systems is taken into consideration in the design, the existing and new

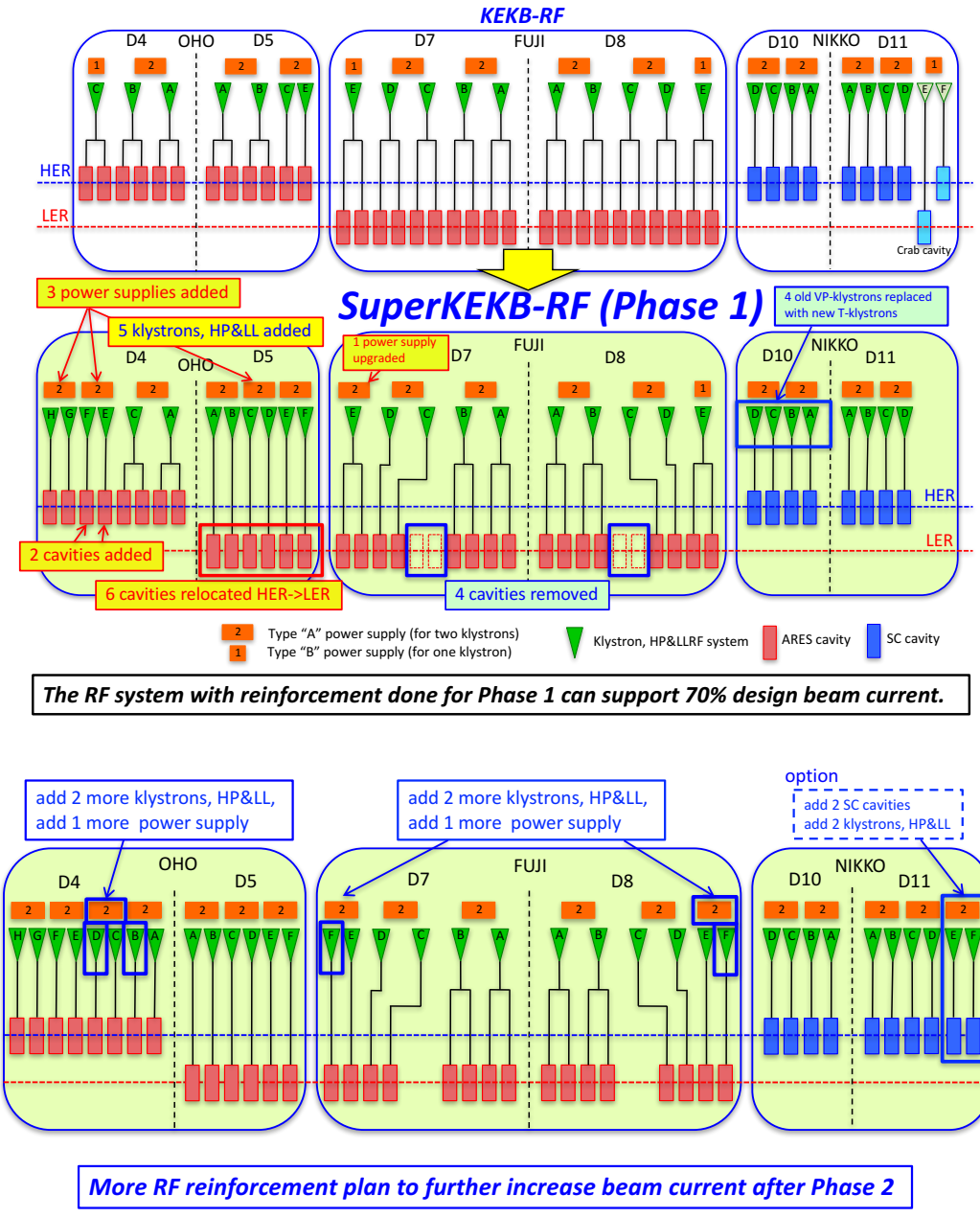

Figure 6.2: (top): The layout of KEKB RF system, (middle): the layout of SuperKEKB RF system for phase 1 commissioning, and (bottom): the layout of SuperKEKB RF system at the ultimate phase.

systems coexist in different RF stations for beam operation without problems. After the beam commissioning, the other analog LLRF systems will be replaced with new digital ones step by step, according to available budget.

In the context of LLRF, two issues need more careful investigation for the higher beam currents: one is the CBI associated with the accelerating mode, and the other is the gap transient effects. In the KEKB operation, the $\mu = -1$ mode instability was observed at around 1 A, even with the ARES and the SCC, and a damper system for the $\mu = -1$ mode was used to suppress the instability. For SuperKEKB with higher beam currents, an improved damper system is needed to have higher damping rate for the $\mu = -1$ mode. In addition, we need to pay attention to the $\mu = -2$ (maybe also $\mu = -3$) modes. A new damper is being developed for a higher damping rate, which will replace the present $\mu = -1$ mode damper used in KEKB. The new damper will be extended for the $\mu = -2$ mode after the beam commissioning. As for the gap transient effects, a new simulation method was developed, where three cavity system of the ARES is taken into account, to evaluate the gap transient-related issues and possible cures. Details of the new digital LLRF system, the CBI damper, and the gap transient evaluation are described in Section 6.4.

Based on these investigations, we have concluded that the SuperKEKB RF system can be constituted by reusing the existing RF system with the ARES and SCC as much as possible with necessary reinforcement and improvements. This strategy passes on the reliability of the KEKB RF system, proven in the long-term operation, and also reduces the construction cost. The reinforcement of the RF system will be performed in phases, as shown in Fig. 6.2, to meet the available budget as well as beam commissioning scenario. During construction period from 2010 to 2014 the RF system will be reinforced from the KEKB RF system (top of Fig. 6.2) to the system matched to the phase 1 commissioning (middle of Fig. 6.2). In the construction phase, five RF stations are added in D4 and D5 of the Oho straight section. And the ARES cavities are rearranged as follows: six cavities in D5 are converted from the HER beam line to the LER, two cavities are added in D4 for the HER, and four cavities in D7 and D8 for the LER are removed. With the new configuration, 14 RF stations are operated with the new scheme where one klystron drives one ARES cavity. Up to about seventy percent of the design beam current can be supported with this configuration. After the commissioning starts, more RF reinforcement will be conducted to increase the beam currents to the design values, as shown in (bottom of Fig. 6.2), depending on machine performance and available budget.

6.2 Normal Conducting Cavity

6.2.1 Preface

Through design investigation on the normal conducting RF cavity system for the SuperKEKB collider based on the nano-beam scheme, we have concluded that the existing ARES cavities developed for KEKB can be reused without modification. It seems to be a conservative solution, however, reliable and consequently economical. In addition, the results of high power tests on the two types of existing HOM loads for the ARES cavity have shown that either type can be reused within each performance limit. On the other hand, the input coupler needs to be upgraded in accordance with the increase in beam loading per cavity.

6.2.2 Introductory Review on ARES scheme

The ARES cavity is a normal-conducting three-cavity system [3] developed for KEKB in order to suppress the longitudinal coupled-bunch instabilities (CBIs) due to large detuning of the accelerating mode from the RF frequency for beam-loading compensation. The acronym "ARES" stands for Accelerator Resonantly coupled with Energy Storage, just representing its RF schematics based on the $\pi/2$-mode operation where an accelerating cavity is resonantly coupled with an energy storage cavity via a coupling cavity in between. Figure 6.3 shows an equivalent kinematic model of three coupled pendulums, where the $\pi/2$ normal mode is used as the accelerating mode. The energy storage cavity, which corresponds to the left-side pendulum with a relatively huge mass, functions as an electromagnetic flywheel to stabilize the accelerating mode by increasing its total stored energy against the beam loading onto the accelerating cavity (the right-side pendulum). By the way, this scheme is inevitably accompanied with two parasitic modes other than the $\pi/2$ mode, namely, the 0 and π normal modes. Moreover, these parasitic 0 and π modes interact with the beam as strongly as the accelerating mode, and would drive severe longitudinal CBIs. In order to avoid this difficulty, the coupling cavity (the middle pendulum) is equipped with a damper selectively acting on the 0 and π modes.

Key features of the ARES scheme based on the $\pi/2$-mode resonant coupling are summarized as follows.

- The stored energy ratio for the $\pi/2$ mode is given by $U_s/U_a = k_a^2/k_s^2$, where U_a is the stored energy in the accelerating cavity and U_s the energy in the storage

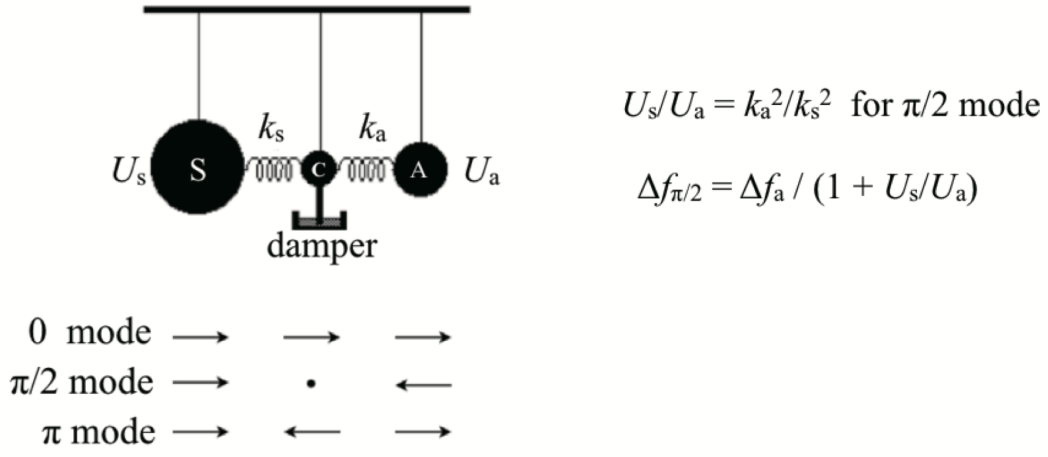

Figure 6.3: Coupled pendulum model showing the ARES scheme.

cavity, k_s the coupling factor between the accelerating and coupling cavities and k_s the coupling factor between the storage and coupling cavities.

- The $\pi/2$ mode shows extraordinary field stability, which assures that the stored energy ratio U_s/U_a can be kept almost constant in the presence of detuning by Δf_a for the accelerating cavity loaded with beam. Therefore, the detuning of the $\pi/2$ mode will be reduced as $\Delta f_{\pi/2} = \Delta f_a/(1 + U_s/U_a)$.
- The parasitic 0 and π modes can be selectively damped by equipping the coupling cavity with a damper.
- Moreover, the damped 0 and π modes are nearly symmetrically located with respect to the RF frequency. Therefore, the impedance contributions from these two modes to CBIs cancel each other out to some extent.

6.2.3 ARES cavity

Figure 6.4 shows the front, side, and top views of the ARES cavity for KEKB, the design of which is based on a concept demonstrator named ARES96 [4]. For a better understanding of this RF structure, a 3D transparent view is also shown in Fig. 6.5, where the half-cell coupling cavity (HCC in Fig. 6.4) is intentionally omitted for simplicity.

The energy storage cavity is a large cylindrical steel structure with dimensions of 1070 mm in diameter and 1190 mm in axial length, whose inner surfaces are electro-

f_{RF}	508.9 MHz	
U_s/U_a	9	
R/Q_0	15 Ω	for the $\pi/2$ accelerating mode
Q_0	1.1×10^5	
V_c	0.5 MV	
P_c	150 kW	60 kW (acc. cav.) + 90 kW (str. cav.)

Table 6.2: RF parameters of the ARES cavity.

copper plated. The Q value of the TE_{013} mode is 1.65×10^5, which is 85% of the theoretical value assuming a copper electrical conductivity of 5.81×10^7 S/m (100% IACS conductivity). The storage and coupling cavities are electromagnetically coupled through a rectangular aperture of 120 mm wide by 180 mm high, and mechanically connected with rectangular stainless-steel flanges. Then, the flange connection is vacuum-sealed by welding thin stainless-steel lips along the perimeter. RF power is fed through an input coupler [5] attached to a drive port of the storage cavity (Fig. 6.5). Details of the input coupler for the ARES cavity are described later, together with its upgraded parts.

The accelerating cavity is a HOM-damped structure in itself, which was carefully designed to be smoothly embedded into the whole ARES scheme without any structural or electromagnetic incompatibilities. The accelerating cavity was fabricated by brazing oxygen-free copper (OFC) parts in a vacuum furnace. Details of HOM damping in the ARES cavity, together with its RF absorbers, are described in a later section. The coupling cavity, also made of OFC parts, is brazed to one side of the accelerating cavity in the horizontal direction. The accelerating and coupling cavities are coupled through a rectangular aperture of 120 mm wide by 160 mm high. On the other side, a half-cell coupling cavity is brazed (front view in Fig. 6.4) in order to restore mirror symmetry with respect to the vertical mid-plane including the beam axis.

A coaxial antenna-type coupler [6] is attached to the central port of the coupling cavity in order to damp the parasitic 0 and π modes (C-damper in Fig. 6.4 or Fig. 6.5). The coupler consists of two coaxial lines crossing at a right angle, where the end of the horizontal coaxial line and the upper end of the vertical one are electrically shorted to form a stub-supported crossing structure. The horizontal coaxial line is equipped with a disk-type alumina RF window as shown by a green disk in Fig. 6.5. The extracted RF power is dissipated as heat in a water-cooled dummy load attached to the lower end of the vertical coaxial line. As shown in Fig. 6.6, the loaded Q values of the 0 and π modes can be reduced to around 100, while the $\pi/2$ mode is not affected.

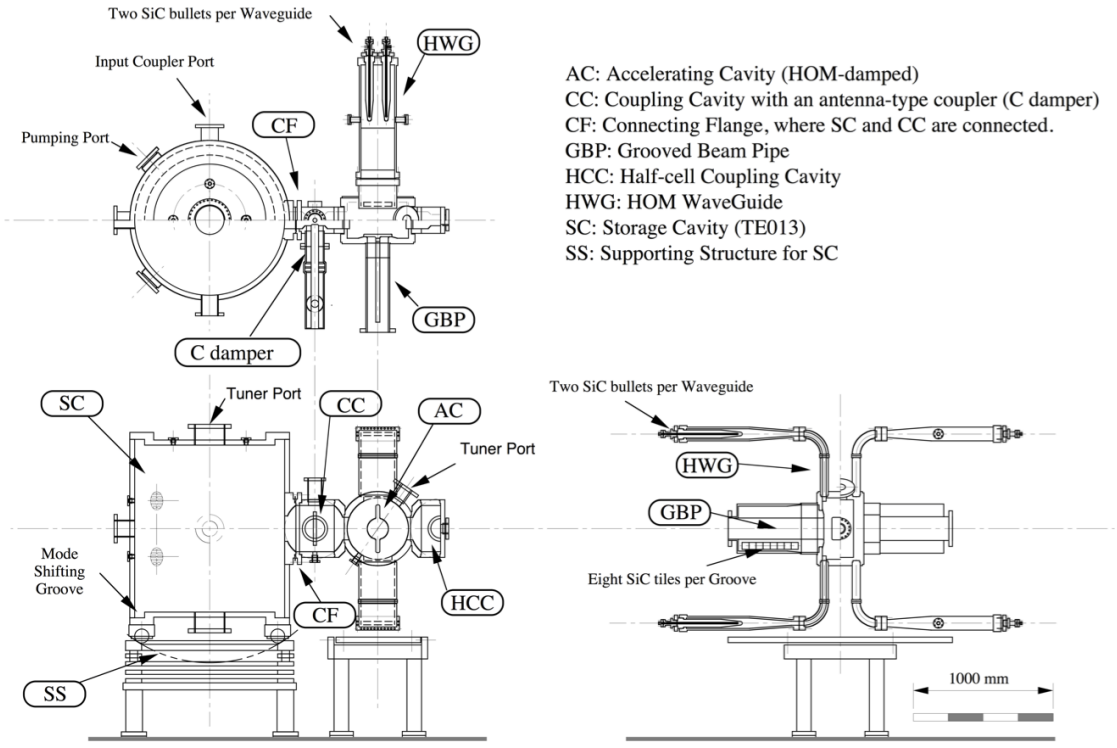

Figure 6.4: Top, front and side views of the ARES cavity.

The RF design parameters for the ARES cavity are listed in Table 6.2. By adjusting the height of the rectangular aperture between the storage and coupling cavities with respect to that between the accelerating and coupling cavities, that is, 180 mm vs. 160 mm as described above, the stored energy ratio U_s/U_a was set at 9. Therefore, the detuning for the $\pi/2$ mode can be reduced by one order of magnitude as $\Delta f_{\pi/2} = \Delta f_a/(1 + U_s/U_a)$. The design cavity voltage of 0.5 MV is generated with a wall loss of 150 kW in total: 60 kW and 90 kW for the accelerating and storage cavities, respectively.

In KEKB, 20 ARES cavities had been successfully operated to store positron beams of up to 2.0 A in the LER, while 12 ARES cavities in combination with 8 super conducting cavities had been used to store electron beams of up to 1.4 A in the HER. Fig. 6.1 (top) shows the whole RF system of the KEKB collider, together with RF-related machine parameters (as of Nov. 15, 2006) for physics run. Many problems had been overcome one-by-one [7]. Roughly, the problems can be divided into two categories: infancy problems, especially with accessory devices being used in long-term operation, and cavity problems attributed to quality control issues, usually associated with the stringent cost goals in the production phase.

Judging from the operational performance of the ARES cavity system demonstrated

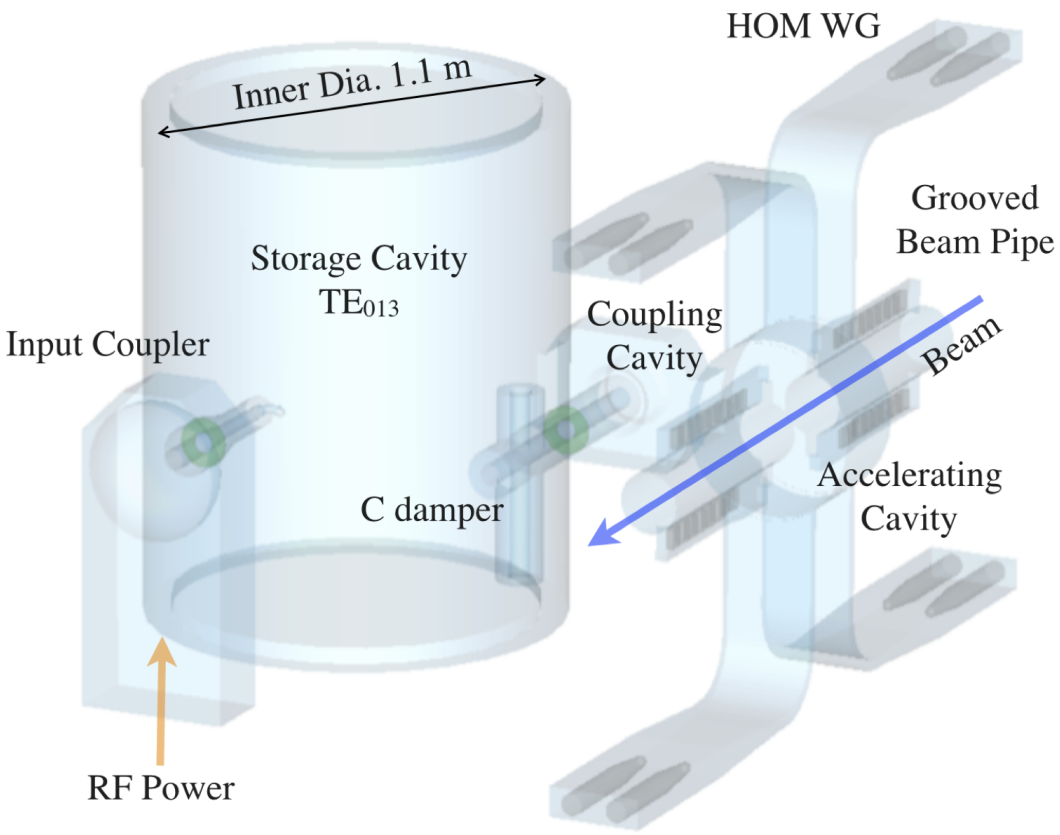

Figure 6.5: Transparent view of the ARES cavity.

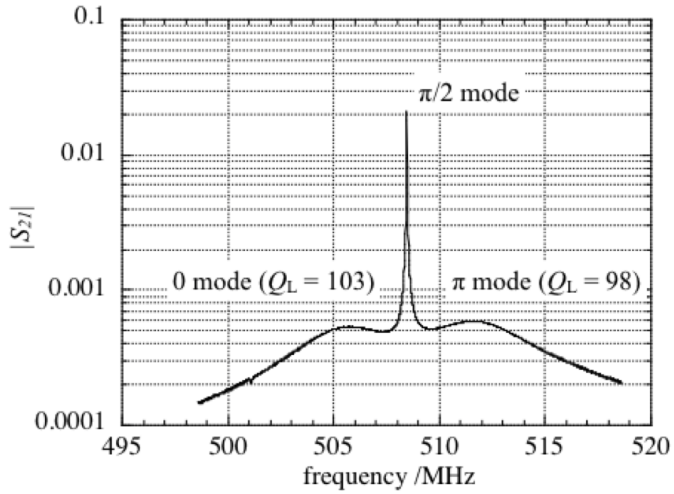

Figure 6.6: Accelerating mode (the $\pi/2$ mode) and the damped parasitic 0 and π modes. The vertical axis shows the transmitted power amplitude $|S_{21}|$ from port #1 at one endplate of the accelerating cavity to port #2 at the other endplate, measured with a network analyzer.

through the KEKB's exploration, together with promising results from high power experiments on the existing HOM loads, we have concluded that the ARES cavity system for KEKB can be reused [8] in the SuperKEKB collider. That is because the nano-beam scheme keeps the design beam currents in both rings within approximately double those achieved in KEKB. It is the input coupler that needs to be upgraded in accordance with the increase in beam loading per ARES cavity.

6.2.4 Fundamental Mode Issues

Figure 6.1 (bottom) shows the whole RF system required for the SuperKEKB collider to achieve the design luminosity of $8 \times 10^{35}\ cm^{-2}s^{-1}$ at its ultimate stage, together with RF-related machine parameters listed as an example. In accordance with the increase of beam power, the number of RF stations each configured as one klystron driving one ARES cavity will be increased up to 14 in the LER and up to 8 in the HER.

Figure 6.7 shows the coupling impedances (real part) of the $\pi/2$ mode per ARES cavity, calculated for two cases. One is for the KEKB LER where a beam current of 1.8 A being accelerated with 20 ARES cavities ($V_c = 0.4$ MV per cavity with the input coupling factor $\beta = 3$). The other is for the SuperKEKB LER where the design current of 3.6 A being accelerated with 22 ARES cavities. For simplicity, it was assumed that every ARES cavity, with the same input coupling factor $\beta = 5$, is to be detuned by the

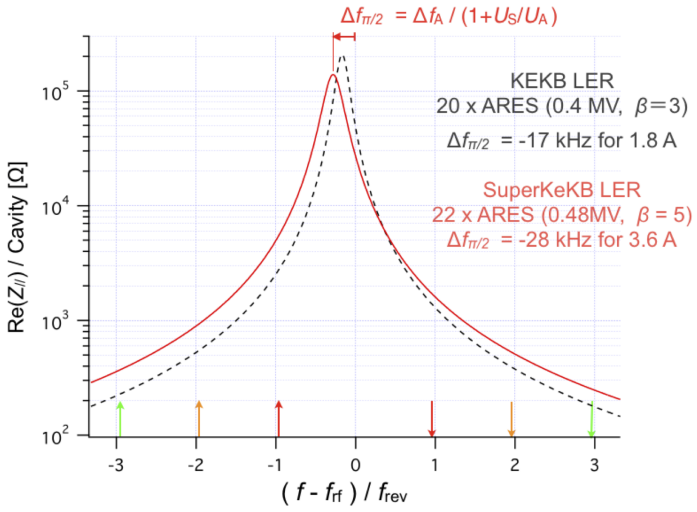

Figure 6.7: Coupling impedance of the $\pi/2$ mode calculated for the SuperKEKB LER where the design beam current of 3.6 A being accelerated with 22 ARES cavities, compared with that for the KEKB LER.

same amount of frequency, independently of whether the RF station is configured as one ARES cavity per klystron or two ARES cavities per klystron. The black dashed and red solid curves correspond to the KEKB and the SuperKEKB cases, respectively. The amount of frequency detuning $|\Delta f_{\pi/2}| = |\Delta f_a|/(1 + U_s/U_a)$ for the $\pi/2$ mode increases from 17 kHz to 28 kHz, however, still being kept below one third of the beam revolution frequency of 99.4 kHz. In addition, the impedance spectrum becomes broad since the coupling factor being increased from 3 to 5. Figure 6.8 shows the growth rates calculated for the -1, -2, and -3 modes of the longitudinal CBI in the SuperKEKB LER due to detuning of the $\pi/2$ mode. Here normal operation condition, where all cavities are powered with no parked cavities out of operation, is assumed. In this case, the growth rates of modes except for the -1 mode are lower than the radiation damping rate. Section 6.4 describes more detail including the cases of other operation conditions and measures.

Another issue concerns longitudinal CBIs arising from the impedance imbalance between the parasitic 0 and π modes. The 0 and π modes are located nearly mirror-symmetrically with respect to the $\pi/2$ mode to be tuned into the vicinity of the RF frequency. Therefore, the impedance contributions from the damped 0- and π-mode resonances to CBI can be counterbalanced between excitation and damping. However, detuning of the accelerating cavity by Δf_a affects the field distributions of the 0 and π modes in the first order. Figure 6.9 shows the coupling impedance (real part) of the damped 0 and π modes calculated for the same cases as above. The impedance

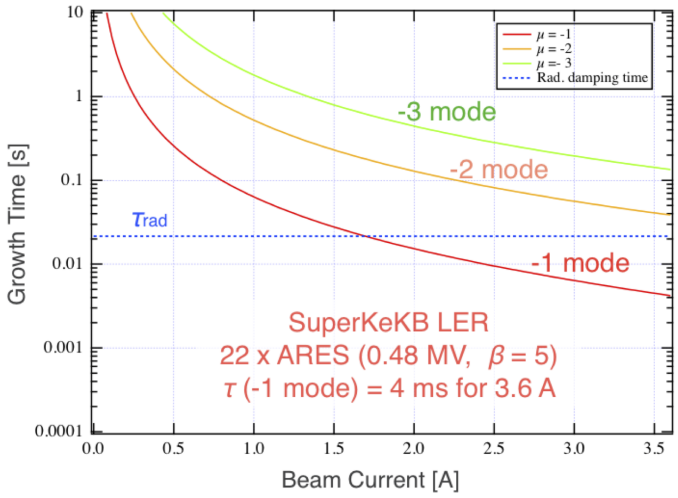

Figure 6.8: Growth time constants of the CBI modes of μ= -1, -2, and -3 due to the $\pi/2$ mode, plotted as a function of the beam current in the SuperKEKB LER.

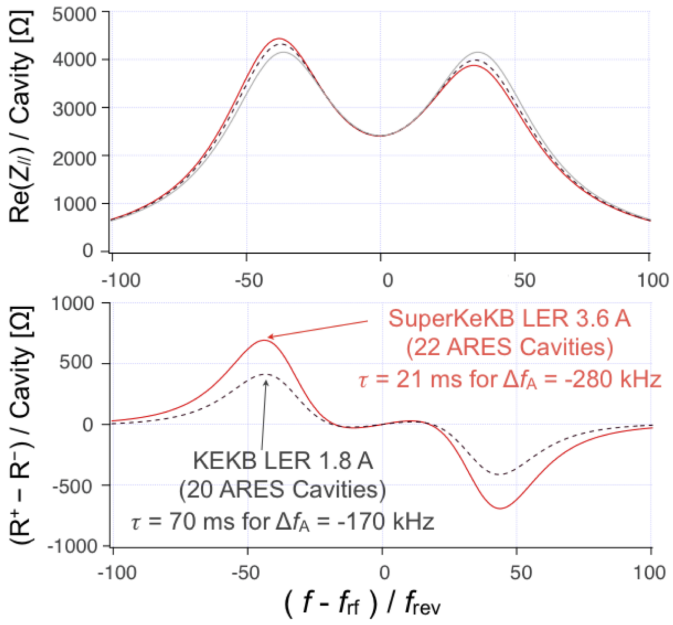

Figure 6.9: Coupling impedance (top) of the 0 and π modes, and the imbalance (bottom) with respect to the RF frequency.

imbalance (the difference between the original waveform and its mirror image obtained by horizontal reverse with respect to the RF frequency) is also shown, where excitation is positive and damping is negative, and the fastest growth time is indicated for each case. This calculation was carried out as follows. The perturbation due to Δf_a was taken into account up to the first order. The external Q value of the coupling cavity to the antenna coupler (C-damper) was assumed to be 50 (the same as for KEKB), which gives $Q_L = 100$ for the unperturbed 0 and π modes with $U_a = U_c$. As the accelerating cavity is detuned downward, the field distribution changes as $U_a > U_c$ for the 0 mode, on the other hand, $U_a < U_c$ for the π mode, where the energy imbalance is proportional to $\Delta f_a/(f_\pi - f_0)$. As for the KEKB LER, the fastest growth time is estimated 70 ms at a beam current of 1.8 A, much slower than the radiation damping time of 21 ms. It is consistent with the fact that any CBI due to the 0 and π modes had not been observed in KEKB. As for the SuperKEKB LER with the design beam current of 3.6 A, the fastest growth time is estimated 21 ms for a CBI mode number around -40, that is about -4 MHz apart from the RF frequency. It is slightly faster than the radiation damping time of 22 ms, however, slow enough for a longitudinal bunch-by-bunch feedback system to cure. It should be noted that the CBI modes arising from the impedance imbalance between the 0 and π modes are usually located out of the frequency band for an RF feedback system to act on the beam through the klystron.

6.2.5 HOM loads

Figure 6.10 shows the HOM-damped accelerating cavity part and close-up views of the two types of HOM loads. Four rectangular HOM waveguides (WGs) are directly brazed to the upper and lower sides of the accelerating cavity in order to damp the monopole HOMs and the vertically polarized dipole HOMs. The extracted HOM power is guided through each waveguide and finally dissipated in two bullet-shaped SiC ceramic absorbers inserted at the WG end (see WG HOM load in Fig. 6.10). The bullet-shaped absorber (55 mm in diameter and 400 mm in length including the tapered head) is directly water-cooled. In order to damp the dipole HOMs deflecting the beam in the horizontal direction, two grooved beam pipes (GBPs) [9, 10] is attached to both endplates of the accelerating cavity. The GBP, with an inside diameter of 150 mm for its circular pipe, has two grooves (dimensions: 30 mm in width and 85 mm in depth) on the upper and lower sides. Inside each groove, there are eight SiC tiles (dimensions: 48 mm $\times$ 48 mm $\times$ 10 or 20 mm) arranged in a line and brazed to a water-cooled copper plate (see GBP HOM load in Fig. 6.10). The details of the HOM loads for the ARES

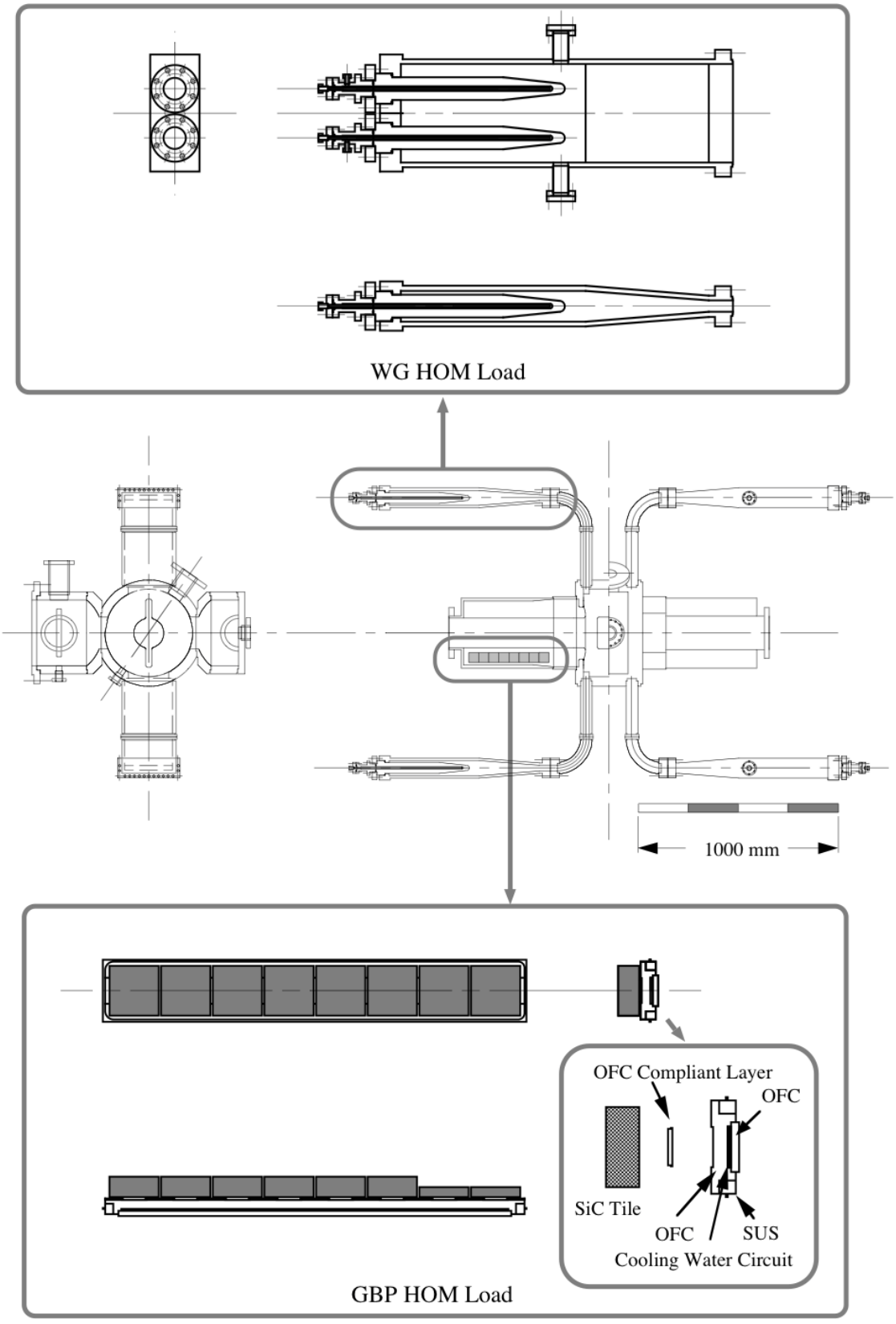

Figure 6.10: Front and side views of the HOM-damped accelerating cavity, and close-up views of the waveguide (WG) and GBP HOM loads.

	KEKB LER Sep. 21, 2004	SuperKEKB LER	Rating[††]	Achieved[†††]
Beam current [A]	1.6	3.6		
Number of bunches	1293	2503		
Bunch length [mm]	7	6		
Loss factor [V/pC]	0.40 (0.39[†])	0.44		
P_{HOM}/ARES [kW]	5.4[†]	17		
P_{HOM}/WG [kW]	1.05[†]	3.3	5.0	20
P_{HOM}/Groove [kW]	0.3[†]	0.93	1.2	1.5

[†]Based on calorimetric measurement.

[††]Continuous power handling rating.

[†††]Maximum power handling capability achieved in experiment.

Table 6.3: HOM power estimates for SuperKEKB LER.

cavity were reported in Ref. [11].

Table 6.3 summarizes the HOM power estimates for the ARES cavity operated in the SuperKEKB LER and the results of measurements in the KEKB LER as a reference. The power handling ratings determined from a set of high power experiments are also listed, together with the records achieved therein. First of all, the total HOM power per cavity is estimated to be 17 kW for the SuperKEKB LER with the design beam current of 3.6 A consisting of 2503 bunches with a bunch length of 6 mm. This value is about three times higher than the reference value of 5.4 kW for the KEKB LER.

The WG load is expected to show excellent power handling capability since the bullet-shaped SiC absorbers with a relatively high thermal conductivity of 125 $\mathrm{Wm^{-1}K^{-1}}$ (at room temperature) are directly water-cooled. Before this SuperKEKB project was launched, a WG load detached from a spare ARES cavity had been tested up to 20 kW (10 kW per absorber) [12, 13]. As part of R&D efforts [14, 15] for the former project aimed at the luminosity enhancement based on 'high-current' scheme, a series of high-power experiments on the WG load had been carried out from 2006 through 2009 at a test stand equipped with an L-band klystron capable of delivering RF power of up to several tens of kilowatts. Figure 6.11 shows the setup of an experiment for measuring the surface temperature distribution along the SiC absorber in situ with use of an infrared thermometer. Conductive heat transfer inside the SiC absorber is dominant over others from its surface to the surroundings by radiation or convection. Therefore, the experiment was carried out in the atmosphere so as to allow us to elim-

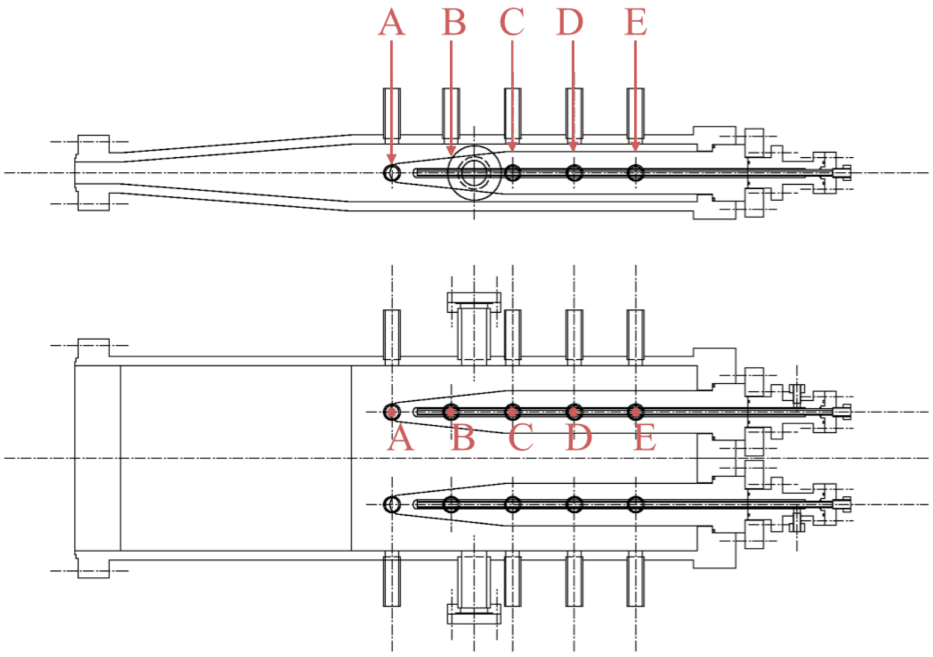

Figure 6.11: Setup for in situ measurement of the surface temperatures (at the points A through E) along each of the bullet-shaped SiC absorbers in a HOM waveguide.

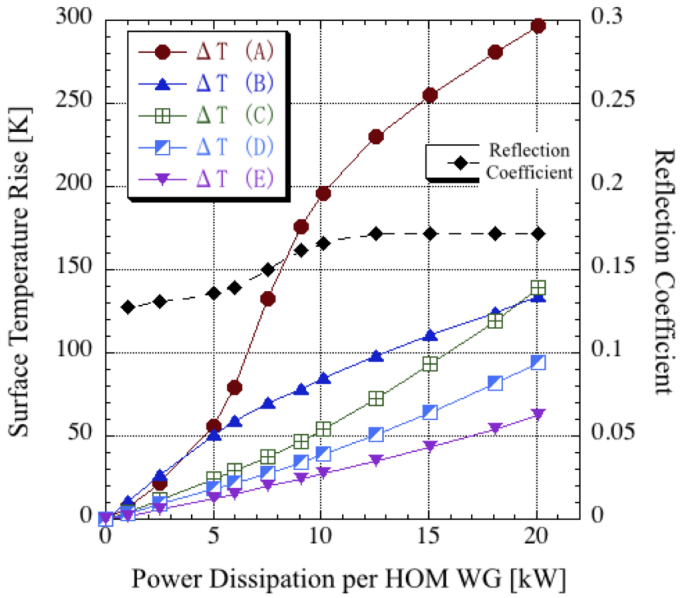

Figure 6.12: Surface temperature rises along a type-96 bullet-shaped SiC absorber for KEKB are plotted as a function of the absorbed power per HOM waveguide, together with the reflection coefficient from the load.

inate systematic errors in temperature measurement. Figure 6.12 is a graph showing the temperature rises at five points along the surface of the absorber (as indicated by letters "A" through "E" in Fig. 6.11), plotted as a function of the absorbed power, together with the reflection coefficient for the WG load. When the absorbed power exceeds 5 kW, the surface temperature around the tip of the nosecone, for which cooling efficiency is not good compared with the rest part, shows a rapid increase, which is accompanied with a small step-like change in the reflection coefficient. Probably, a positive feedback loop can explain this phenomenon: increased temperature around the tip of the nosecone leads to increased dielectric constant there which leads to locally increased RF power absorption therein [12]. The small step-like change in the reflection coefficient might be explained in the following way: excessive temperature rise at the tip of the nosecone leads to non-uniformity in dielectric constant along the nosecone section, which resulted in increased RF shockwave arising from there. In order to suppress the excessive temperature rise at the tip, a new bullet-shaped SiC absorber (type 06 in Fig 6.13) with improved cooling efficiency especially for the nosecone section was developed and successfully tested up to 20 kW [12] as shown in Fig 6.14. However, according to Table 6.2, the power handling capability of the existing absorber (type 96 in Fig. 6.13) is enough for use in the SuperKEKB collider based on the nano-beam scheme. Conservatively, the continuous power handling rating for the WG load should be set at 5 kW (2.5 kW per absorber). This rating still leaves a margin of 50% with respect to the HOM power estimate of 3.3 kW (Table 6.2).

Since the SiC tiles for the GBP load are indirectly cooled (Fig. 6.10), we should pay more attention to the effect of the absorber temperature on the reflection coefficient and the vacuum pressure. Therefore, we carried out a series of experiments with two different setups. Figure 6.15 shows the setup of our first experiment using a standard rectangular waveguide (WR650). As shown in Fig 6.16, a GBP load unit was fit into a rectangular opening at the top wall of the waveguide chamber and fixed thereto and hermetically sealed by TIG welding. Figure 6.17 shows the setup for our second experiment, which was devised to reproduce the actual electromagnetic boundary conditions as faithfully as possible. A GBP was detached from a spare cavity by cutting, and a fitting flange was attached to the machined end face by TIG welding. The GBP chamber thus prepared was connected to a rectangular waveguide port via a custom-made waveguide transformer (Fig. 6.18). Every flange-to-flange joint was made vacuum-tight with use of a metal gasket. Figure 6.19 shows a graph summarizing the results of the two experiments, where the vacuum pressure and the VSWR are plotted as a function of the absorbed power normalized per groove (or per GBP load unit). In the first experiment, the vacuum pressure rapidly increased when the absorbed power exceeded

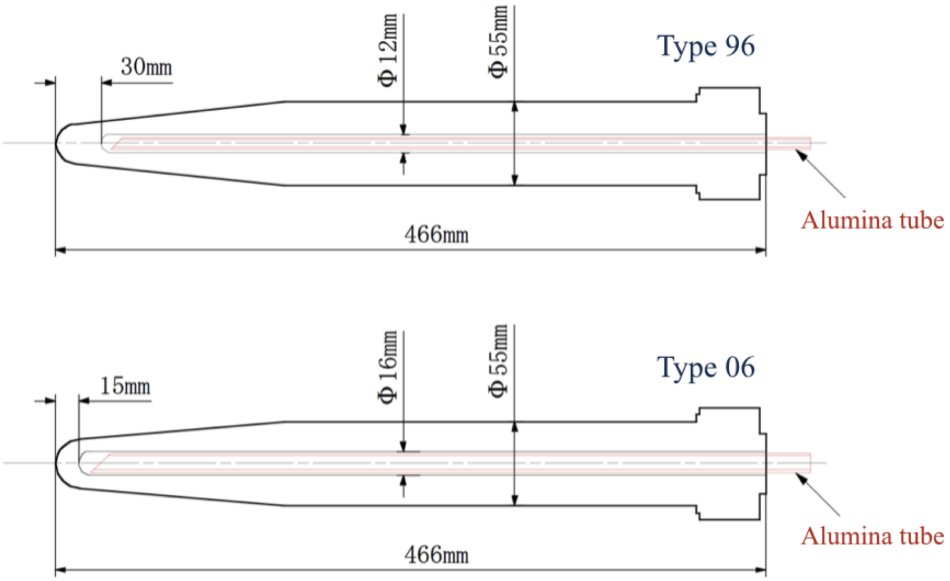

Figure 6.13: Newly developed type-06 bullet-shaped SiC absorber (bottom), compared with type-96 (top) for KEKB.

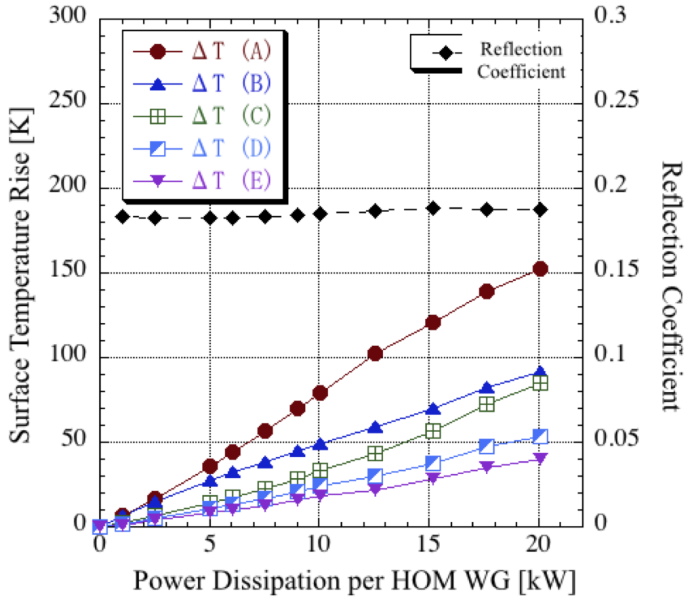

Figure 6.14: Surface temperature rises along a newly developed type-06 bullet-shaped SiC absorber are plotted as a function of the the absorbed power per HOM waveguide, together with the reflection coefficient from the load.

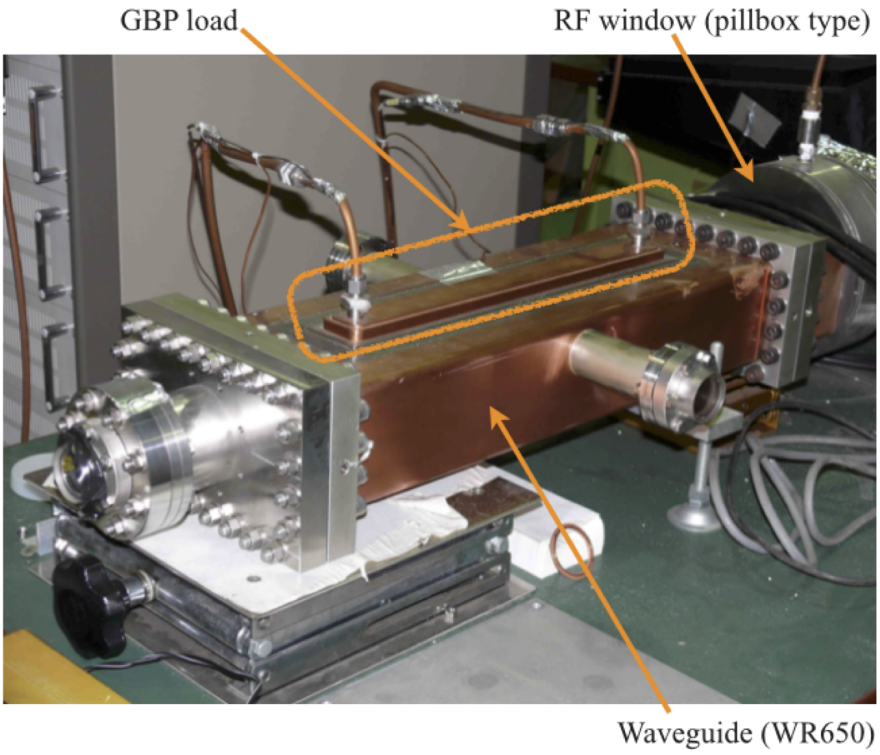

Figure 6.15: Setup for high-power testing of a GBP load unit, placed inside a standard rectangular waveguide at L band.

1.2 kW, but no electric discharge inside the waveguide chamber was seen through a viewing port. What was worse, RF conditioning over a long time proved ineffective for mitigating this phenomenon. On the other hand, in the second experiment, the response of the vacuum pressure was smooth up to 1.5 kW per groove. So far, we have no clear evidence to answer what brought this distinct difference in vacuum pressure response. It might be due to accidental sample-to-sample variation in performance, or due to the systematic difference in electromagnetic boundary conditions. Probably, the latter case gives a higher limit than the former. Although further investigation with more samples is needed, for the time being we should adopt a limit of 1.2 kW per groove as the power handling capability for the GBP load. This limit still leaves a margin of 29% since the estimated HOM power is 0.93 kW per groove.

6.2.6 Input Coupler

The ARES cavity is fed with RF power through one input coupler attached to a drive port of the storage cavity (Fig. 6.5). The power handling capability of the input coupler

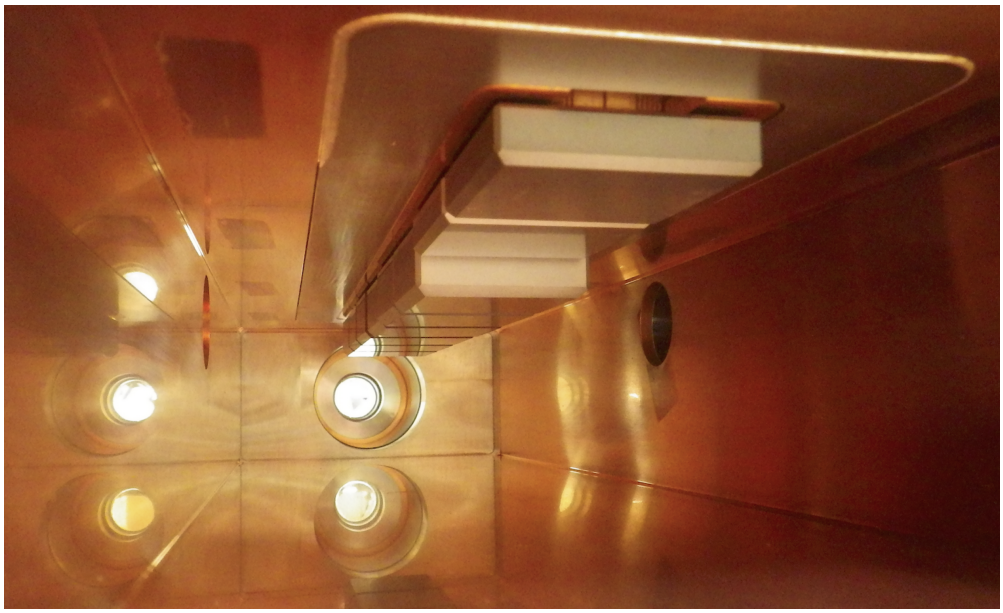

Figure 6.16: Inside of the rectangular waveguide (Fig. 6.15) with a GBP HOM load unit (Fig. 6.10) attached on the ceiling.

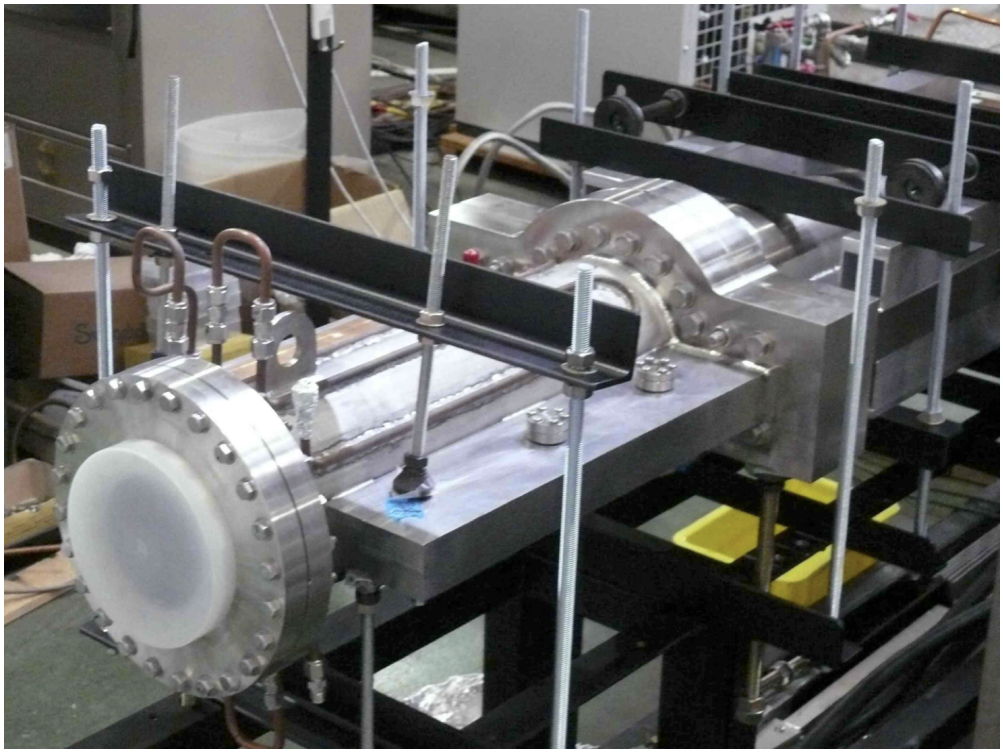

Figure 6.17: Setup for high-power testing of a GBP unit, detached from a spare cavity and modified to flange-mount type.

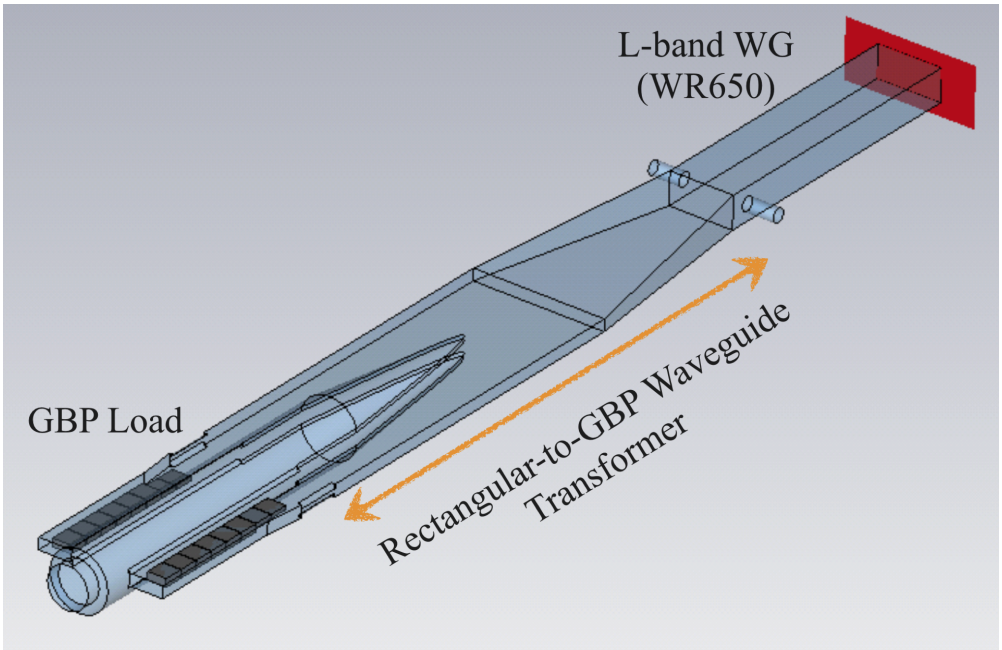

Figure 6.18: Waveguide transformer from a standard rectangular waveguide to a GBP unit with 8 SiC tiles per groove.

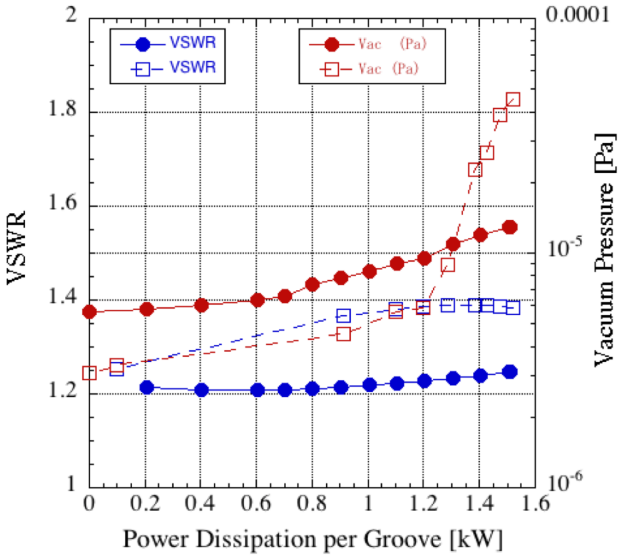

Figure 6.19: Vacuum pressure (red) is plotted as a function of the absorbed power per groove (or per absorber unit of 8 SiC tiles): open rectangles for an absorber unit placed inside a standard rectangular waveguide and closed circles for a GBP unit detached from a spare cavity, together with the VSWR response (blue) for each case.

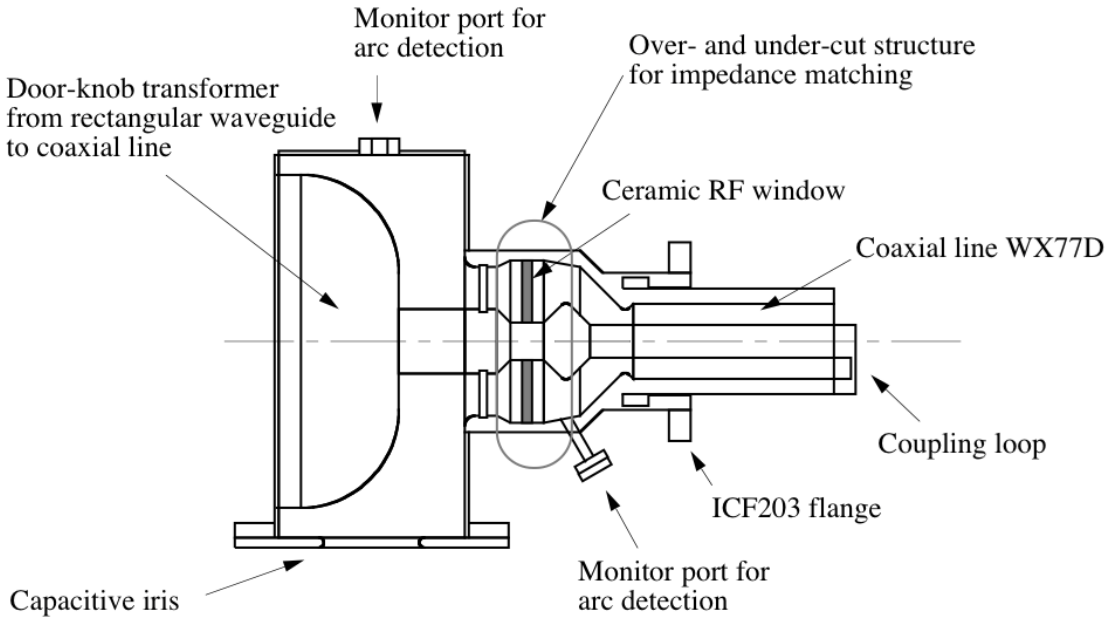

Figure 6.20: Input Coupler for the ARES cavity.

needs to be upgraded in accordance with the increase of RF input power (including a wall power of 150 kW for generating a cavity voltage of 0.5 MV) from 400 kW (KEKB design) to 750 kW for RF stations each configured as one klystron driving one ARES cavity. The good news to our upgrade considerations was that some input couplers for KEKB had been tested up to 950 kW [5] in 1997, surpassing the above design value.

Figure 6.20 shows a schematic drawing of the input coupler [5] for the ARES cavity. The RF power is transmitted from the rectangular waveguide input, via a doorknob transition with a capacitive iris, to the coaxial line with a disk-type alumina window. The coaxial line is tapered down and ends with a magnetic coupling loop. The input coupling factor to the cavity can be adjusted by rotating the loop angle with respect to the direction of the magnetic field, and becomes maximum when the magnetic field is perpendicular to the loop. However, the maximum input coupling factor attained with the KEKB-type coupler was limited below 3.2, while an input coupling factor over 6 is required for the SuperKEKB. Then, we decided simply to extend the coupling loop into the cavity. Figure 6.21 shows the results from measurements using a cold model (Fig. 6.22) of input coupler attached to a spare ARES cavity. The input coupling factor is plotted as a function of the loop height, easily changed for the cold model by replacing copper spacers. The response of the unloaded Q value of the $\pi/2$ accelerating mode is also shown. Accordingly, the loop height was extended from 17 mm (KEKB) to 60 mm, which gives an input coupling factor over 6 with enough margin while being accompanied with a decrease around 3% in the unloaded Q value. In addition, some

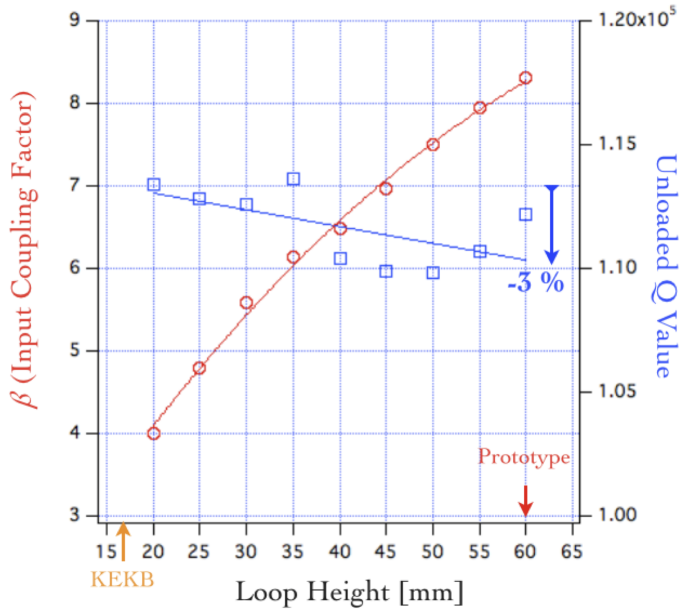

Figure 6.21: Input coupling factor, measured using a cold model, is plotted as a function of the loop height, together with the unloaded Q value of the $\pi/2$ mode.

improvements have been applied to the input coupler for more stable operation. Fine grooving inside the outer conductor (Fig. 6.23) of the coaxial line (WX77D) proved quite effective in suppressing the multipactoring discharge occurring there [16].

In June 2010, a prototype input coupler for SuperKEKB, with the input coupling factor set at 6.4 (cold), was tested at the RF station D5-C (see Fig. 6.1: top), in which one klystron drove one ARES for the KEKB HER. Figure 6.24 shows the forward and reflected RF power (red and green, respectively) together with the vacuum pressure (black) in the cavity, plotted as a function of the HER beam current. About 750 kW of RF power was successfully fed through a single coupler, 130 kW for generating a cavity voltage of 0.47 MV and 610 kW delivered to the beam. Thus, the performance of the prototype input coupler was successfully demonstrated under the practical operating conditions probably expected to be similar to those in SuperKEKB.

Following three input couplers fabricated as the pre-production model in JFY 2010 and 2011, the production of input couplers was started and is underway: 6, 10 and 4 input couplers in JFY 2012, 2013 and 2014, respectively. From the prototype to the production model via the pre-production, some minor changes were made in stepwise to the metal fittings brazed to the alumina disk in order to improve the fabrication yield of the RF windows [17]. So far, 13 input couplers have been processed up to

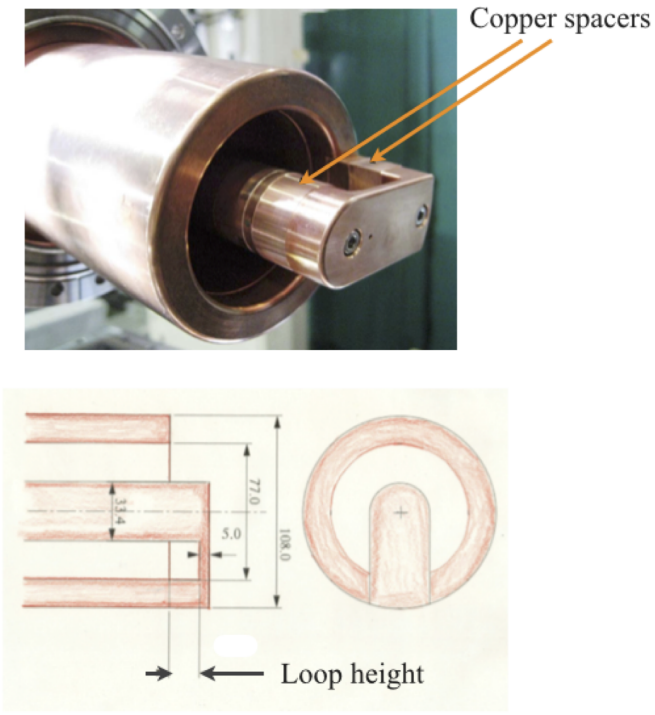

Figure 6.22: Cold model of input coupler.

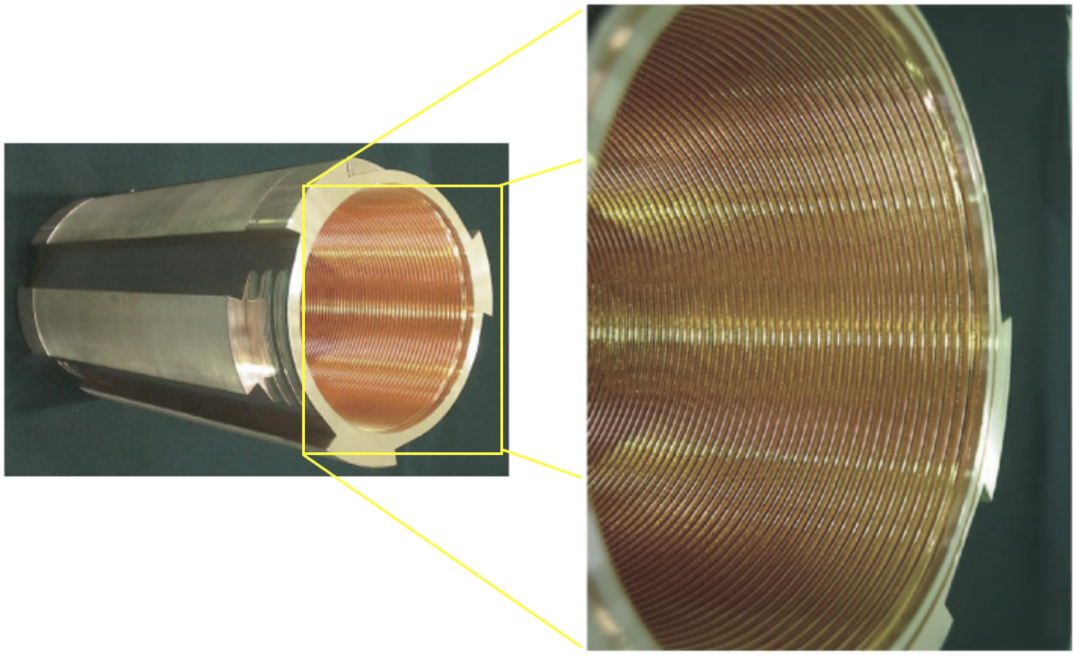

Figure 6.23: Fine grooving inside the outer conductor of the coaxial line WX77D (Fig. 6.17) to suppress multipactoring discharge.

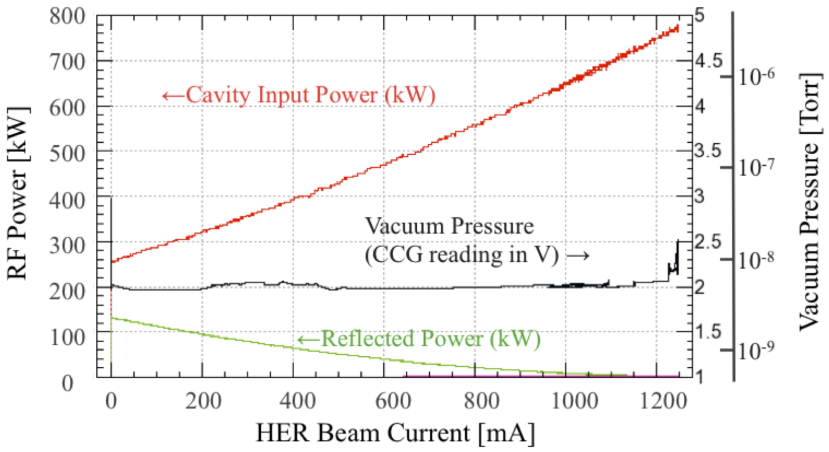

Figure 6.24: Forward and reflected RF power and vacuum pressure for the ARES cavity at the RF station D5-C, equipped with a first prototype input coupler for SuperKEKB.

750-800 kW in a high-power test stand (Fig. 6.25). This test stand was constructed using a spare storage cavity in order to reproduce the operating conditions expected in SuperKEKB as faithfully as possible [18]. Since April 2013 when a dedicated ozonized-water generator became available, ozonized water rinsing of the RF window, followed by vacuum baking, has been our standard pretreatment before high power testing. This pretreatment, which had been applied to some KEKB input couplers for elimination of multipactoring discharge at the RF window [19], has proved effective also in suppressing vacuum pressure spikes during RF conditioning as shown in Fig. 6.26, and consequently shortened the net total time of high-power testing for one input coupler from 100 hours to 70 hours.

KEKB-type input couplers are to be replaced with upgraded ones for 14 RF stations each configured as one klystron driving one ARES cavity for the initial stage of SuperKEKB. Before the phase 1 beam commissioning of the rings, 10 input couplers in the OHO section are to be replaced: 6 and 4 in sections D5 and D4, respectively. In the summer shutdown right after the phase 1 commissioning, 4 input couplers in the FUJI section are going to be replaced.

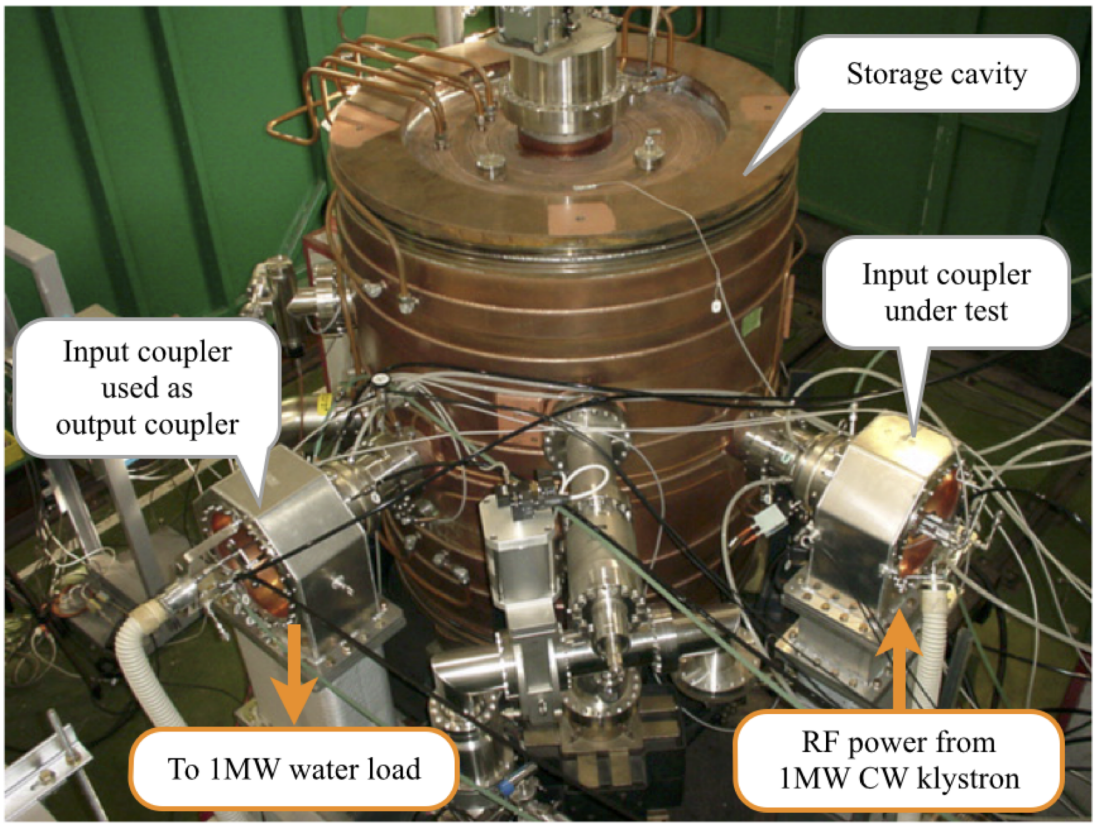

Figure 6.25: Setup using a storage cavity for high-power testing of the input coupler, where another coupler is attached and the extracted RF power is dissipated in a dummy load.

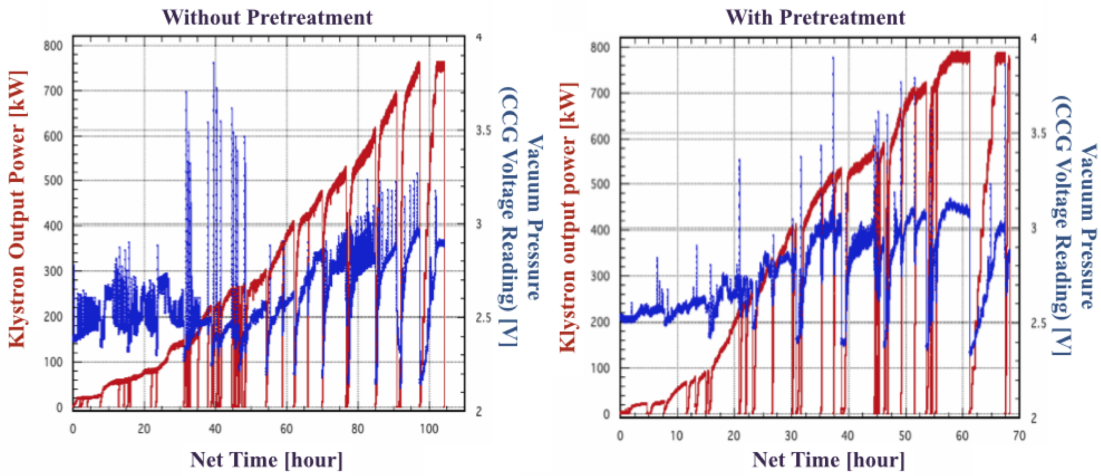

Figure 6.26: RF processing history for an input coupler pretreated with ozonized water rinsing followed by baking (right) is compared with that for another input coupler without pretreatment (left).

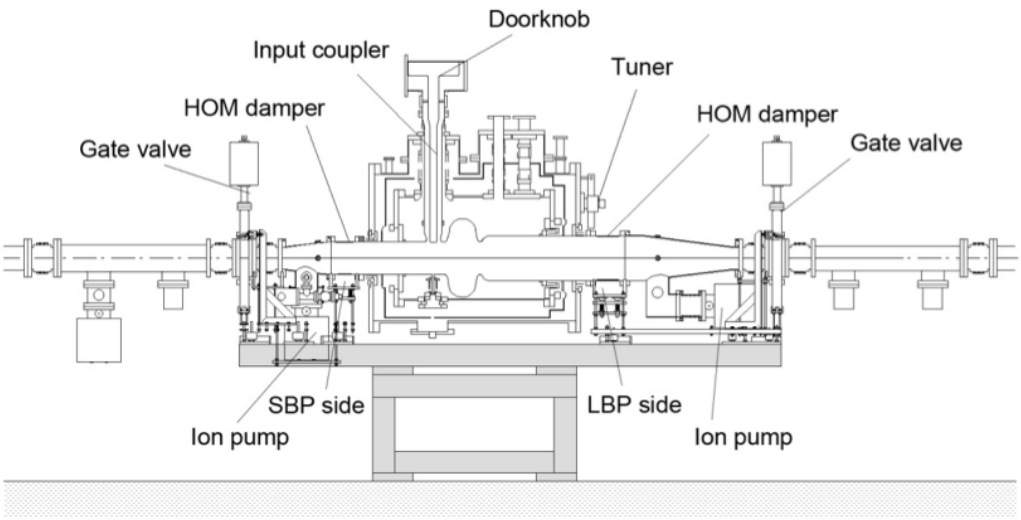

Figure 6.27: Schematic diagram of the superconducting cavity.

6.3 Superconducting Cavity

6.3.1 Superconducting Cavities

Superconducting accelerating cavities have been developed for the KEK B-factory (KEKB) to accelerate the electron beams in the high energy ring (HER) [20]. The cavity has a 509 MHz single cell to provide the accelerating voltage of 1.5 MV at 4.4K. A schematic diagram of the cavity is shown in Fig. 6.27. The first four cavity cryomodules were installed in December 1998 and commissioned. The other four were installed in the summer of 2000 [21]. Figure 6.28 shows the cryomodule installed in the KEKB tunnel. Those eight cavities were operated until the machine shutdown (June 2010). Those superconducting cavities will be re-used at SuperKEKB. The design parameters, achieved values at KEKB and required values at SuperKEKB are listed in Table 6.4.

In order to accelerate the beam current of 2.6 A, measures for beam instabilities are important. The large stored energy of the cavity, which is 7.6J at the voltage of 1.5 MV, suppresses the frequency detuning for the optimum tuning well below the beam revolution frequency. The large stored energy also contributes to suppress the phase oscillation due to a long bunch train gap. The higher order mode-induced coupled bunch instabilities also should be avoided. Large beam pipes and two ferrite HOM dampers are applied to the SCC [22]. One of the HOM dampers is attached on a small

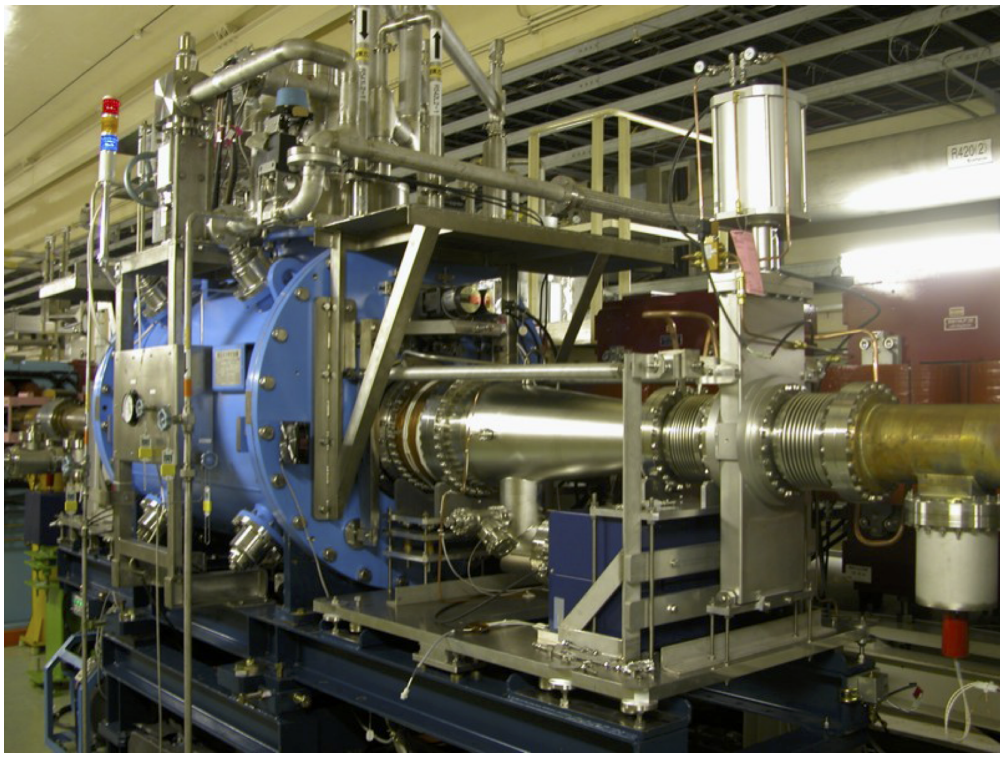

Figure 6.28: Cryomodule installed in the KEKB tunnel.

Parameter	KEKB (design)	KEKB (achieved)	SuperKEKB
Beam energy (GeV)	8.0	8.0	7.0
Beam current (A)	1.1	1.4	2.6
Bunch charge (nC)	2	10	10
Bunch length (mm)	4	6	5
RF voltage (MV)	1.5	1.2-2	1.5
Beam power (kW/cavity)	250	400	400
HOM power (kW/cavity)	5	16	37

Table 6.4: Design parameters, achieved values at KEKB, and required values at SuperKEKB.

Frequency (MHz)	508.9
R/Q (Ω/cavity)	93
Gap length (m)	0.243
Diameter of iris (m)	0.220
Geometrical factor (Ω)	253
Field ratios*	
E_{acc}/V_c (m^{-1})	4.11
E_{sp}/V_c (m^{-1})	7.65
E_{sp}/E_{acc}	1.84
H_{sp}/E_{acc} (G/(MV/m))	40.3
Total cryomodule length (m)	3.701
Volume of Liq. He (L/module)	290
Static loss (W)	30
HOM damper size (mm)	
SBP	4t $\times$ 220ϕ $\times$ 120
LBP	4t $\times$ 300ϕ $\times$ 150
Maximum HOM impedance	
TM011 (kΩ)	2
TM110 (kΩ/m)	37
Loss factor for σ=5 mm (V/pC)	1.37 V/pC

* V_c, E_{acc}, E_{sp} and H_{sp} are accelerating voltage, accelerating field, surface peak electric field and surface peak magnetic field, respectively. E_{acc} is defined as $E_{acc} = V_c/L$, where L is the gap length.

Table 6.5: Geometrical parameters of the cavity module.

beam pipe (SBP damper), while the other is attached on a large beam pipe (LBP damper). The HOM dampers heavily damp the Q factors of the HOM's. Geometrical parameters of the cavity module [23] are listed in Table 6.5.

An antenna type coaxial input coupler is attached to deliver the beam power of 400 kW [24]. The inner conductor is made of copper and cooled with water. A TiN-coated ceramic disk seals the vacuum and supports the inner conductor. The optimum external Q factor (Q_{ext}) was first set to 70000 for the designed parameters at the beginning of the KEKB operation. This value was changed to 50000 for the higher current operations than the design beam current. We adjusted the coupling by inserting the inner conductor using a 4 mm thinner metal gasket at the inner conductor joint. The input and reflected RF power as a function of beam current are shown in

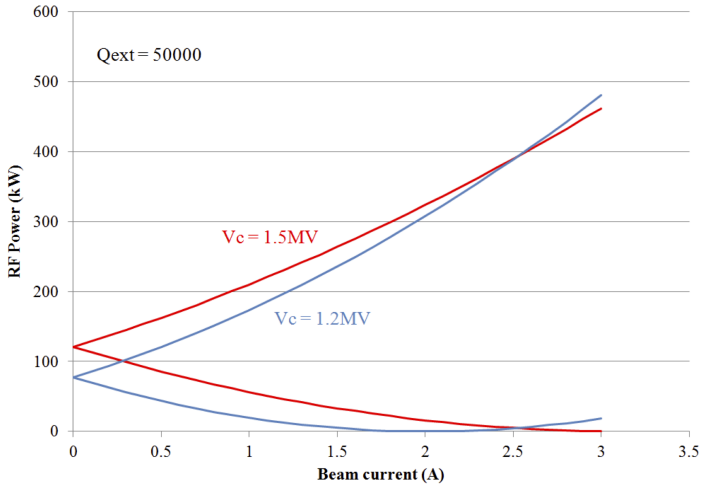

Figure 6.29: Input and reflected power as a function of beam current.

	Without SiC (kW)	With SiC (kW)
Backward radiation	1.3	1.4
Forward radiation	15.7	4.0
SBL damper	8.6	9.5
LBP damper	11.7	12.8
Total	37.4	27.7
SiC damper (240mm)	-	26.1

Table 6.6: Calculated HOM power loads with and without SiC damper at the beam current of 2.6A.

Fig. 6.29 for the cavity voltage of 1.5 MV and 1.2 MV with the Q_{ext} of 50000. The optimum Q_{ext} for the operation at SuperKEKB is 60000, however, the present Q_{ext} is applicable since the reflected power is less than 10 kW at the beam current of 2.6 A. Even if the lower cavity voltage operation is required (1.2 MV, for example), the present Q_{ext} is still acceptable. Therefore, further coupling adjustment is not needed for SuperKEKB.

The HOM dampers attached on the beam pipes absorb the beam-induced HOM power. The dampers successfully absorbed the HOM power up to 16 kW without any troubles at the KEKB operation. However, the HOM power will increase to 37 kW at the design beam current of SuperKEKB. It is rather difficult to absorb such large HOM power in the present HOM dampers. Measures for the large HOM power absorption have to be taken [25], as described in the next section.

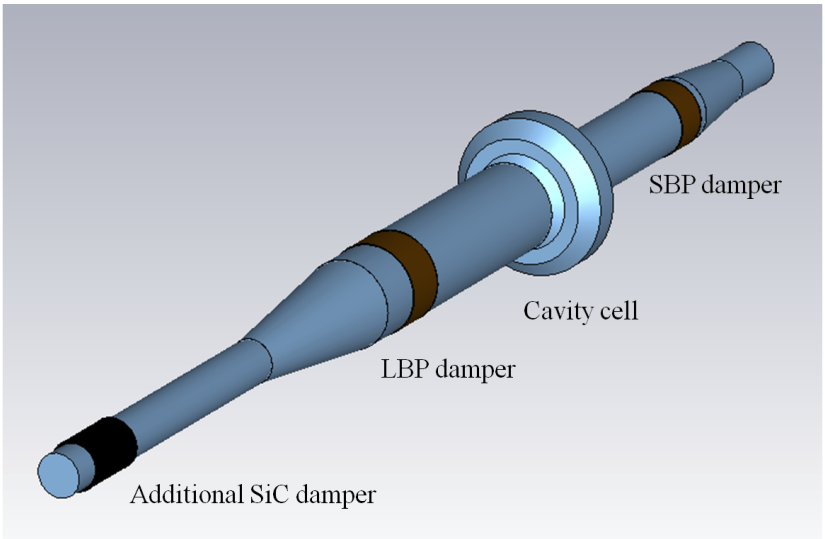

Figure 6.30: Geometry used in the power flow calculation of the CST-PS solver.

6.3.2 Measures for Large HOM Power

The most serious issue of the cavity operation at SuperKEKB will be the large HOM power. The expected HOM power is 37 kW per cavity at the 2.6 A operation with a bunch charge of 10 nC. The present HOM dampers may absorb the HOM power, however, the temperature rise of the ferrite increases the outgas rate that may trigger the high voltage breakdown of the cavity. Reduction of HOM power loads is necessary.

Recently, a new power flow calculation of the HOM power was developed using the Computer Simulation Technology: Particle Studio (CST-PS) wake field solver. With this method the absorbed power at each HOM damper can be calculated. The results showed that the HOM power load on each damper is not as high as that expected before, but a significant amount of HOM power is radiated to the downstream through the beam pipe. The radiated HOM power becomes a power load on the cavities in the downstream. The calculation results also showed that an additional HOM damper on the beam pipe could absorb the radiated HOM power. Results of the damper load calculation with and without the additional SiC damper of 240 mm in length are listed in Table 6.6 for the beam current of 2.6 A. Figure 6.30 shows a geometry used in the CST-PS solver. With the additional HOM damper, the present ferrite HOM dampers can absorb HOM power without difficulties and the radiated HOM power becomes acceptable for the cavities in the downstream. Furthermore, the additional damper can be attached on the beam pipe outside the gate valve without vacuum breaking of the cavity, so that we can avoid the risk of particle contamination.

The R&D of the additional HOM dampers is ongoing to optimize its size and setting position. The SiC material was chosen for the additional damper because the fabrication of this size is established for the normal conducting cavities, and its outgas rate is low compared to the ferrite material. Prototype SiC dampers have been fabricated for the high power testing.

6.3.3 Performance Recovery

In the long term operation at KEKB, the Q factors of several cavities significantly degraded at 2 MV with strong field emission. The degradation was mainly caused by the particle contamination at repairs of indium joints or gasket exchange of the input couplers. The performance of the degraded cavities is still acceptable for SuperKEKB, since the required operating voltage is 1.5 MV. However, further degradation may cause serious problems in the long-term operation. Therefore, performance recovery is desired.

The high pressure water rinsing (HPR) is an effective method to clean the particle contamination. However, in order to apply the usual HPR, the cavity has to be disassembled from the cryomodule. Furthermore, re-assembly of the cavity after the HPR makes another risk of leakage at the indium joints or metal gaskets. If the HPR can be directly applied to the cavity in the cryomodule, we can save time and costs for the disassembly, and avoid the risk of leakage at re-assembly.

Therefore, we have developed a horizontal HPR (HHPR), which can be directly applied to the cavity in the cryomodule [26]. This method uses horizontal insertion of a high pressure water nozzle and an aspirator pump inlet through the beam pipe. Figure 6.31 shows a schematic diagram of the HHPR. The aspirator pump is used to evacuate the wasted water. We started R&D in 2009 using a test cavity, then established this method. In 2012, the HHPR was applied to recover the performance of a spare cavity, which was degraded at the repair of the indium joints. The HHPR was applied to clean the cavity cell and iris for 15 minutes. The Q factors before and after the HHPR are shown in Fig. 6.32; the Q factor was successfully recovered by the HHPR. This cavity was installed in the HER of SuperKEKB. Following this success, the HHPR was also applied to another degraded cavity. The Q factor at 2 MV was drastically recovered from 2×10^8 to 1.3×10^9.

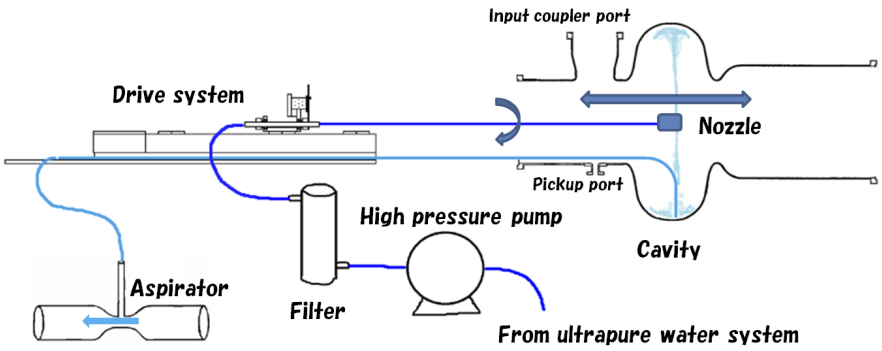

Figure 6.31: Schematic diagram of the horizontal HPR system.

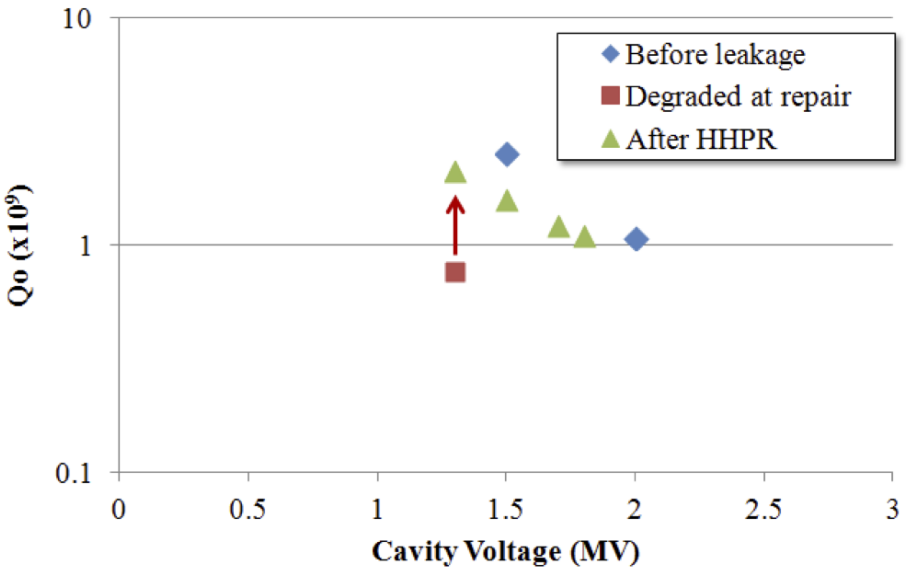

Figure 6.32: Q factors before the helium leakage, after the degradation and after the horizontal HPR.

6.4 Low Level RF Control System

6.4.1 Preface

The existing analog-based LLRF system had been operated stably for KEKB [27]. While they can also be used for SuperKEKB, a new digital LLRF system is being developed for higher accuracy and flexibility. In the design of the new LLRF system, compatibility between the existing and new systems was taken into consideration, so that both systems coexist in different RF stations without problems for the beam operation. This strategy enables us to replace the existing system with the new system step by step, which matches the construction plan with available budget. Furthermore, it allows us to have timely improvements on the new system based on experiences in future beam operation.

A prototype of the new LLRF system was fabricated, and a high power test was performed with an ARES cavity. Good performance of the prototype one was confirmed in the test, and mass production started. Before the Phase 1 commissioning, the analog LLRF systems of nine RF stations for the ARES in the OHO straight section will be replaced with new digital ones. After the beam commissioning, the analog LLRF systems of other RF stations will be replaced with new ones step by step, according to available budget. Meanwhile, a new digital LLRF for the SCC will be developed; basically it has the same functions as the new LLRF for the ARES has, but modifications are needed for the tuner control and interlock system for the SCC. Details of the new digital LLRF system is described in Sec. 6.4.2.

Other improvements required for SuperKEKB LLRF system include: upgrading of the RF reference distribution and stabilization system and upgrading of the dampers to suppress longitudinal coupled-bunch instability (CBI) associated with the accelerating mode of cavities. A new RF reference system is being constructed by using "Phase Stabilized Optical Fiber" and optical transceivers. A new CBI damper has been developed to meet the requirements for higher damping rate as well as capability of curing the $\mu = -2$ and -3 modes in addition to the $\mu = -1$ mode. Finally, gap transient effects and possible mitigations were investigated with an advanced simulation tool, which treats the transient behavior of the three-cavity system of the ARES. These topics are described from Section 6.4.3 to Section 6.4.5.

6.4.2 New Digital LLRF System

Design concept

The new LLRF control system for SuperKEKB consists of μTCA-standard platformed FPGA boards and Programmable Logic Controller (PLC) [28]. They have PowerPC CPU's running on Linux-OS and an EPICS-IOC is embedded in each of them [29], which can be operated remotely via EPICS-Channel Access. The FPGA's perform RF signal control such as feedback (FB) control and cavity tuning like hardware modules, while the parameters for the RF control are provided from EPICS records. The PLC, for which the Yokogawa FA-M3 series is adopted, has two CPU modules: one is a normal logic controller and the other is a linux-OS CPU (F3RP61); the former behaves as a monitoring recorder and slow-interlock system for cooling water flow, temperature, vacuum and so on, while the latter performs as an EPICS-IOC. The operation sequences such as cavity-start up and auto-conditioning are run by EPICS-sequencers embedded in the PLC. For new graphical user interface, the CSS-BOY [30] is adopted as development and runtime environment.

A block diagram of the new digital LLRF control system for an RF station for the ARES cavity in the SuperKEKB main ring (MR) is shown in Fig. 6.33. It includes digital feedback loops for the cavity field and tuner control. Figure 6.34 shows a picture of the new LLRF system for one RF station, housed in three 19"-racks. The main components for the RF signals are installed in the left-side rack, whereas the middle and the right racks accommodate the PLC unit, GUI, arc sensors, vacuum control, etc. Figure 6.35 shows a picture of the μTCA digital control unit. It has five FPGA boards: Digital FB Controller (DFBCNT), Tuner Controller (TNRCNT), Interlock Controller (INTLCNT), RF-Detector Monitor (RFDETMON) and Arc-discharge Monitor (ARCMON). Figure 6.36 shows monitored RF signals and connections between the FPGA boards.

System components and control mechanics for LLRF control

Figure 6.37 shows a block diagram of the FPGA implemented in the DFBCNT board. In this system, in-phase and quadrature (I/Q) components of RF signal are handled for vector control, instead of the amplitude and phase. Therefore, the driving RF is controlled by using an I/Q modulator as shown in Fig. 6.33. The I/Q handling method is one of the most standard techniques for digital RF control in recent days. Required stability and regulation accuracy in the accelerating field is typically $\pm 1\%$ in amplitude

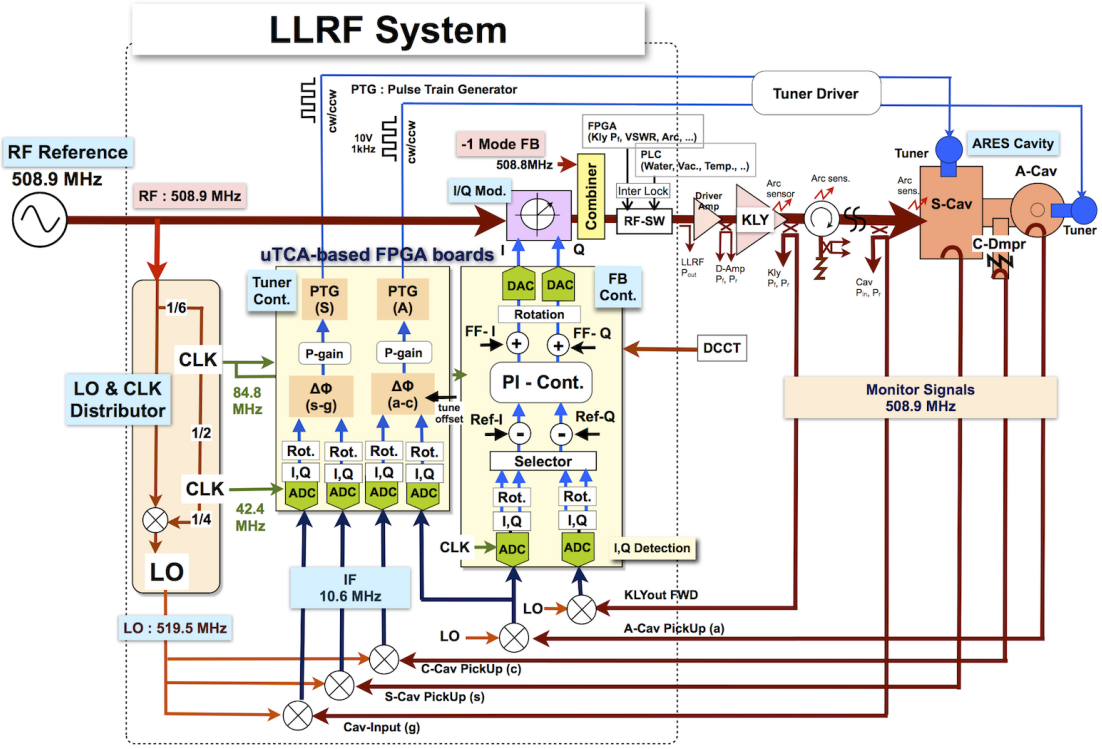

Figure 6.33: Block diagram of the new digital LLRF including the ARES cavity FB control and tuning control. Instead of the amplitude and phase control, the I/Q components of the RF signals are digitally handled by FPGA's.

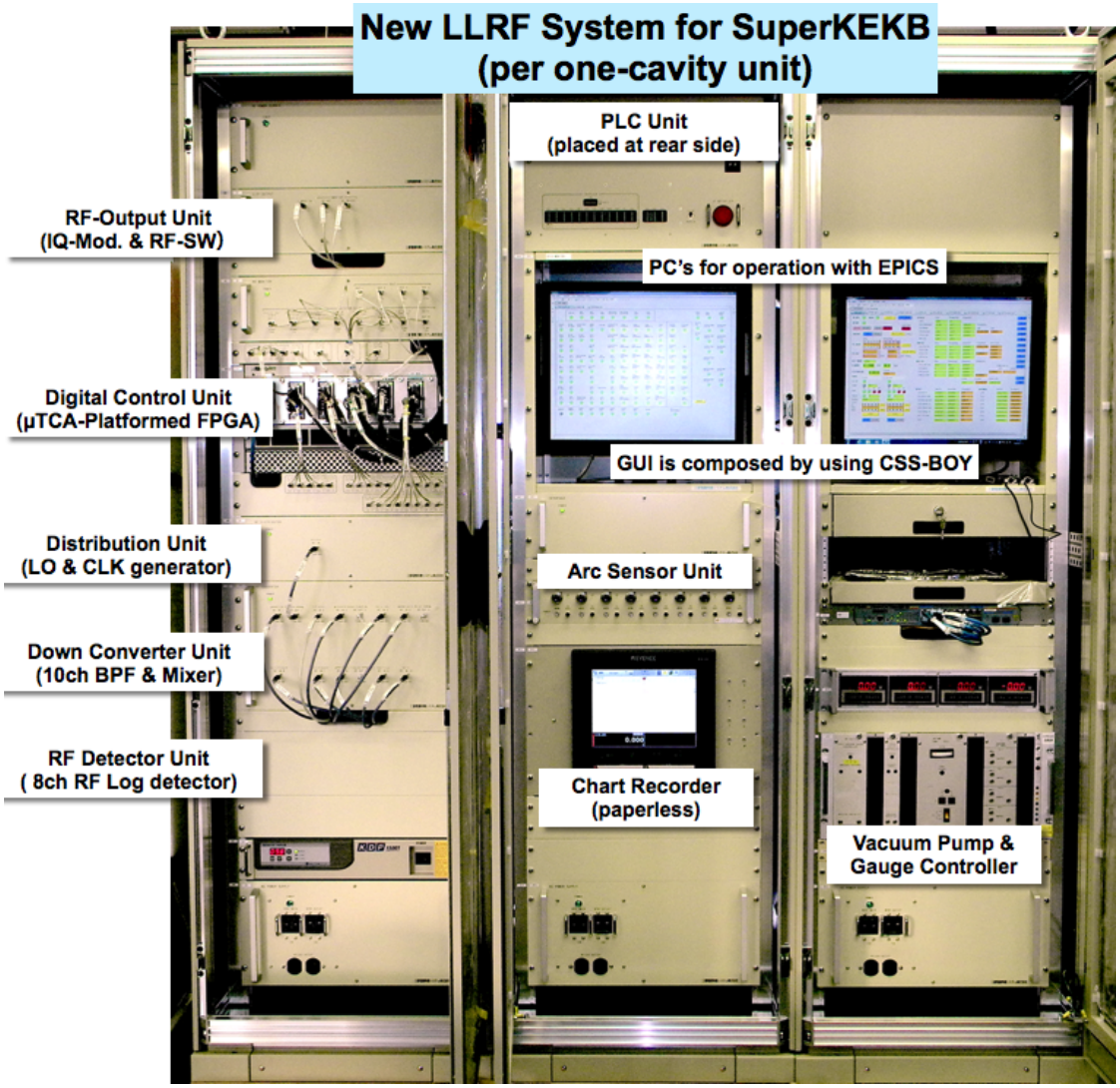

Figure 6.34: Photo of LLRF System for the SuperKEKB for one klystron.

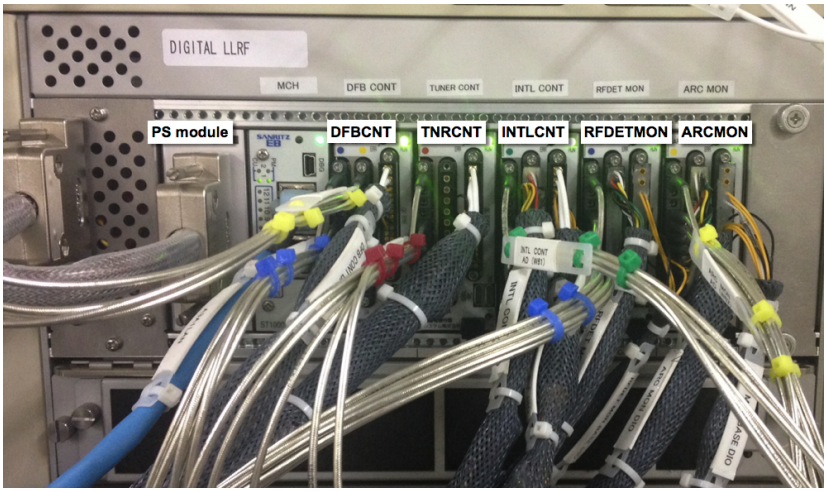

Figure 6.35: Digital LLRF Unit which consists of five FPGA boards based on μTCA-standard platform.

and ± 1 degree in phase. But target values for the new LLRF control system are set $\pm 0.3\%$ and ± 0.3 degrees (both are peak-to-peak values) in the amplitude and phase, respectively, including long term stability such as thermal stability. Then the required resolutions of the amplitude and phase control are less than 0.1% and 0.1 degrees, respectively.

The RF monitor signals (508.9 MHz) are down-converted into 10.6 MHz IF signals with a LO signal (519.5 MHz). The IF signals are sampled by 16-bit ADC's on the FPGA board at quadruple frequency of the IF, so that the I/Q components are directory obtained (see Fig. 6.37). In this sampling method called the I/Q-sampling, the DC component and the second harmonic can be cancelled [31], and both of the orthogonal components of the vectors are almost ideally separated with each other for high-purity wave signal. Consequently, they can be more accurately measured for any vector (any phase) within the dynamic range of the ADC compared with the amplitude and phase detection method. In addition, the phase calibration is simplified by calculating the vector rotation. The LO and clock signals for these boards are generated in the Distribution Unit (in the left rack in Fig. 6.34) from the reference RF signal.

In the DFBCBT board, proportional-integral (PI) FB control is digitally applied to both of the sampled I/Q components in parallel, and the control signals are output from the 16-bit DAC's to the I/Q modulator, as shown in Fig. 6.37. A selector chooses one of the klystron output and cavity pickup signal to perform the FB control loop. The parameters for the IIR digital filters implemented in the loop are also switched by the selector accordingly, to the values optimized to each loop. The DFBCNT also

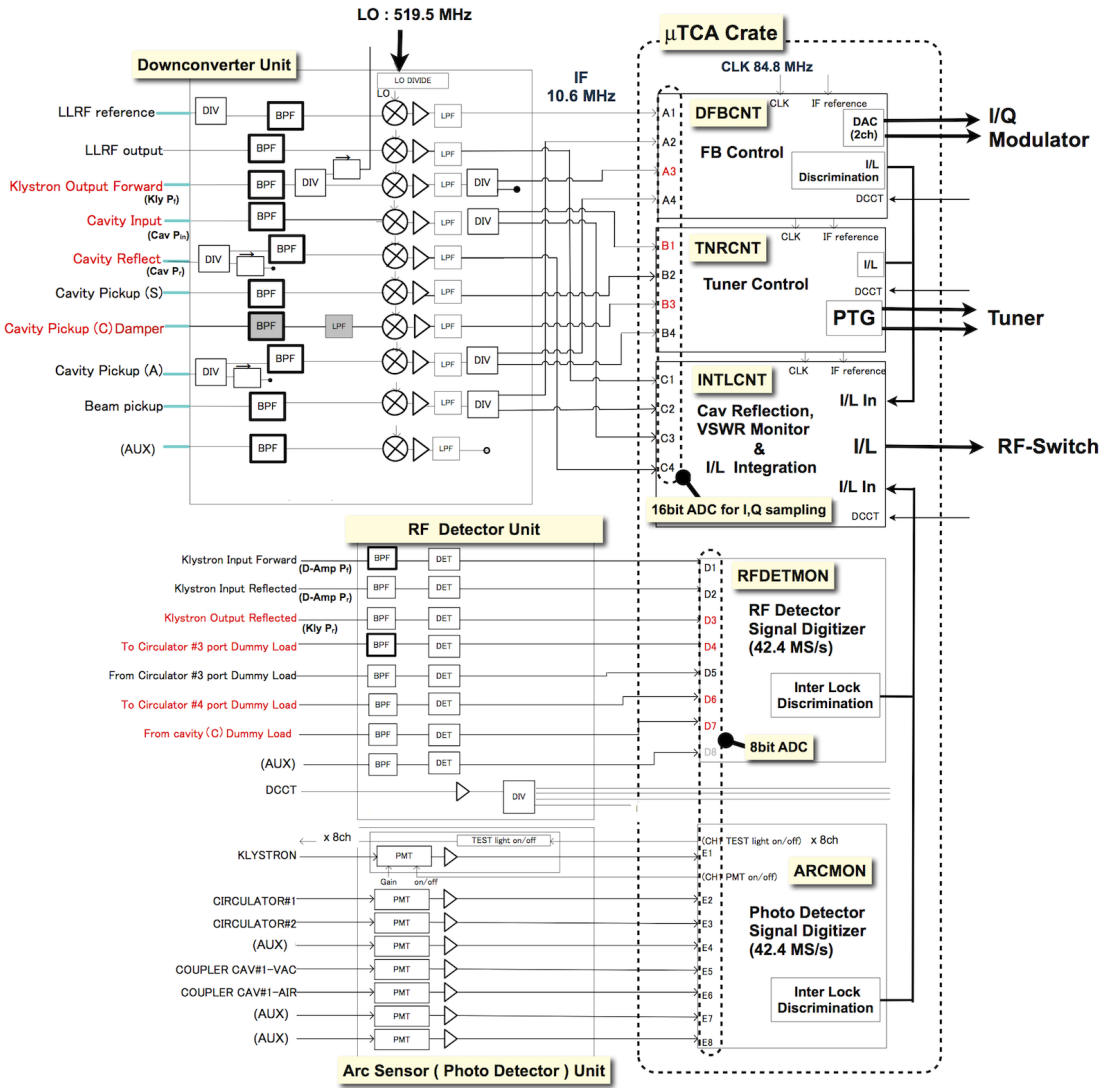

Figure 6.36: Monitored RF signals and connections between the FPGA's.

detects the klystron output power for the interlock. In addition, a klystron phase lock function is implemented in the FPGA, as described later.

Furthermore, the DFBCNT is equipped with measures to cure possible issues related to the high stored beam current. One is that the I/Q offsets or feed-forward (FF) parameters can be flexibly controlled for beam loading compensation according to the beam current measured by a DCCT. Another is related to suppression of the CBI associated with the accelerating mode. As shown in Fig. 6.33, the mode FB signal coming from a mode damper is combined with the FB control signal. The $\mu = -1$ mode damper used in KEKB is reported in Ref. [1]. A new damper for SuperKEKB, which treats not only the $\mu = -1$ mode, but also the $\mu = -2$ and -3 modes, will be described in detail in Sec. 6.4.4. On the other hand, the direct FB control loop used in the analogue LLRF system is not adopted in the new digital LLRF system, because the new system is expected to have sufficiently wide band and precision in the feedback control.

The TNRCNT board controls two tuners of the ARES, one is for the storage (S-) cavity and the other is for the accelerating (A-) cavity. It monitors the cavity input signal and three pickup signals of the S-, C-, and A- cavities of the ARES, and calculates the tuning phases of the S- and A- cavities from these signals. Then it generates pulse trains to drive the tuner motors according to the tuning phases, as shown in Fig. 6.36. Theoretical approach for the tuning control of ARES cavity has been studied in Ref. [32]. The FPGA in the TNRCNT board also has a function to control a piezo tuner of the SCC, for future use of the new digital LLRF to replace the existing analog LLRF system for the SCC.

The INTLCNT board switches RF power off when any abnormal operation sign is detected. It monitors the IF signals with the I/Q-sampling of the input and reflect RF power and calculates the VSWR. The interlock request signal also comes from the other four boards to the INTLCNT board, as shown in Fig. 6.36. Each of three FPGA boards, DFBCNT, TNRCNT and INTLCNT, has 16-bit 4-channel ADC's and 16-bit 2-channel DAC's. The RFDETMON and ARCMON have eight 14-bit ADC's each, and acquire waveforms of RF log detectors and photo-detectors, respectively, at 42.4 MS/s like an oscilloscope. An arc-sensor unit has photo-detectors made of photo-multiplier-tubes. Large-core optical fibers of 600 μm diameter are used to transfer discharging flash from the cavity to the arc-sensors.

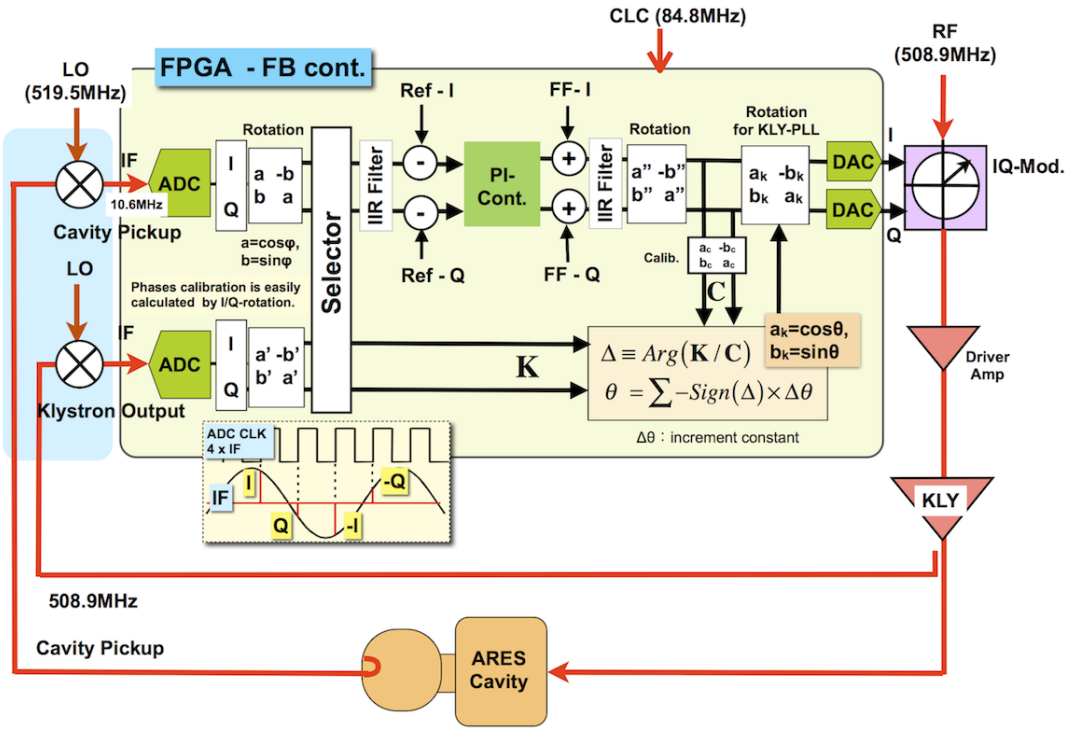

Figure 6.37: Block diagram of FB control and klystron phase lock loop in the DFBCNT. RF monitor signals are down-converted into IF signals and sampled by ADC's at 4-time frequency of the IF (I/Q-sampling). PI-FB control is applied to the I/Q components separately for vector control.

Klystron phase lock loop

The klystron anode voltage is controlled depending on the driving RF power to reduce collector loss for high efficiency [33]. In a high power test, a phase shift of 80 degrees of the klystron output was observed due to the anode voltage change. Such a large phase shift will invalidate the I/Q based FB control; according to our calculation and simulation, an acceptable phase shift for the I/Q based FB control is approximately within ± 50 degrees in our operation condition, which was consistent with the high power test result.

In order to solve the problem, a klystron phase lock loop (KLY-PLL) is implemented in the DFBCNT, as shown in Fig. 6.37. For the KLY-PLL, an additional phase-rotation function is inserted before the DAC outputs to the I/Q modulator. The klystron phase is detected and compared with the FB-output phase as the reference. The total phase shift of the klystron, "θ" in the figure, is accumulated by an increment constant to cancel the phase shift, and then the phase rotation parameters ($\cos\theta$ and $\sin\theta$) are given dynamically by a preset table in 2-degree steps with linear interpolation. The required loop band is less than 1 kHz, because the response of the anode voltage control is only about 1 Hz.

LLRF performance evaluation

The FB control stability was evaluated by an "out-of-loop" measurement in the high-power operation. The results for short term stability and regulation resolution is shown in Fig. 6.38. This figure shows the amplitude and phase of the cavity-pickup signal under FB-control measured by using an RF detector and a mixer, respectively, which are acquired in a oscilloscope for 4 ms time duration. Some small beat is seen in the phase, though it is negligibly small for our specification. In the whole, sufficiently good stability was obtained: the regulation resolution in r.m.s is 0.02% in amplitude and 0.02 degree in phase.

Figure 6.39 shows phase noise spectrum of the ARES cavity pickup signal under FB control in the frequency range from 10 Hz to 10 MHz. The signal source used for this measurement was Agilent E8663D-UNY. The noise is reduced above 10 kHz due to the frequency property of the ARES cavity which has a high-Q value. Sufficiently low noise characteristic was achieved: the time jitter obtained from integral of this spectrum is 71 fs (rms), while the source signal has a 60 fs (rms) time jitter in the same integral region.

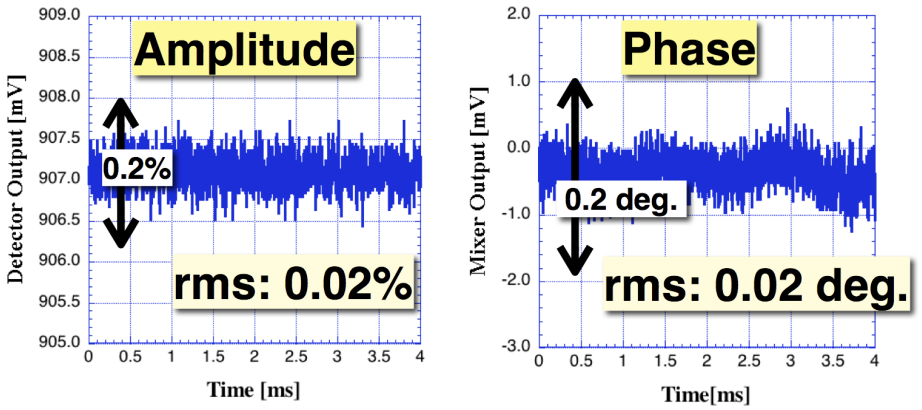

Figure 6.38: Short-term amplitude and phase stability under the FB control evaluated by an out-of-loop measurement. Obtained regulation resolution (r.m.s) is 0.02% in amplitude and 0.02 degree in phase.

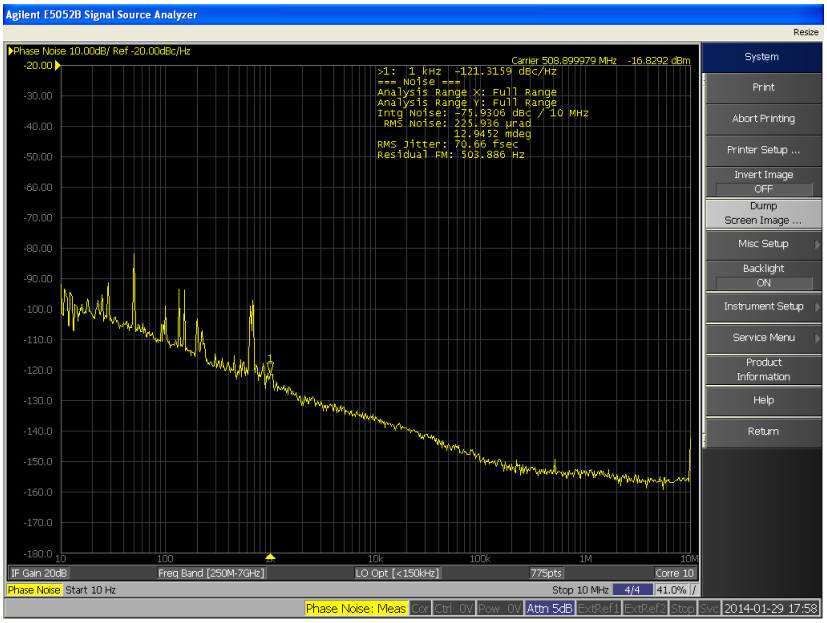

Figure 6.39: Phase noise spectrum of the ARES cavity pickup signal under the FB control (10 Hz $\sim$ 10 MHz). The time jitter obtained by integral of this spectrum is 71 fs (rms), while the source signal has a 60 fs (rms) time jitter in the same integral region.

Disturbance rejection characteristics inside the closed loop is shown in Fig. 6.40. The disturbance such as klystron noise or fluctuation is assumed in this evaluation. Modulation magnitude and phase response at base band are plotted for various FB-gains (P: proportional gain, I: integral gain). The values of P and I in the figure are just setting values in this specific digital system. The real FB gains for continuous system (P_0, I_0) have following relations: $P_0 = P/8$ and $\mathrm{I}_0 = I \times 2^{-15} \times$ CLK, where CLK is 85 MHz.

The solid lines indicate calculated transfer functions for the tuned cavity, and the circle marks are measured data in a high power test including the klystron property. A good agreement is seen between the calculation and measurement. The disturbance noise reduction around 10$\sim$30 kHz is approximately -10 dB: this frequency range is about the same as the bandwidth of the ARES. The response characteristics for beam loading are almost similar with the data shown in Fig. 6.40. The effect of synchrotron oscillation ($\sim$2 kHz) is reduced to approximately -20 dB by the FB control. On the other hand, the effects of revolution ($\sim$100 kHz) such as the bunch gap transient simply conform to the cavity response. The amplitude and phase modulation due to the bunch gap transient can be effectively eliminated by neither the FB nor FF control of LLRF, because the bandwidth of klystrons is about 100 kHz and the bandwidth of the loop is less than 100 kHz corresponding to the group delay of longer than 1 μs, which are much lower than 1 MHz needed for the compensation.

Temperature characteristics for long-term stability is also important. Our target values for the stability are less than $\pm 0.3\%$ in amplitude and ± 0.3 degrees in phase, respectively. Since temperature change during operation with air conditioning is typically ± 2 deg. C, the acceptable temperature coefficient is about 0.1%/deg. C in amplitude and 0.1 deg. /deg. C in phase, respectively. From measurements of temperature characteristics of components in the LLRF, it was found that band pass filters (BPF) implemented in the down-converter units are the most dominant for thermal stability. However, the BPF is indispensable for the LO generation and pick-up RF monitoring in our system. In order to improve the thermal stability, cavity type BPFs were chosen instead of lumped-constant circuit type ones, because the cavity type one has smaller scattering in characteristics for different manufacture lots. Furthermore, fine tuning was applied to every BPF; an example of the results is shown in Fig. 6.41. After the fine tuning, the phase property was significantly improved. Although the amplitude property was slightly degraded in this specific case shown in Fig. 6.41, it is sufficiently small both before and after the tuning. Since the amplitude and phase properties are not independent, an iteration work of the adjustment is needed to optimize both

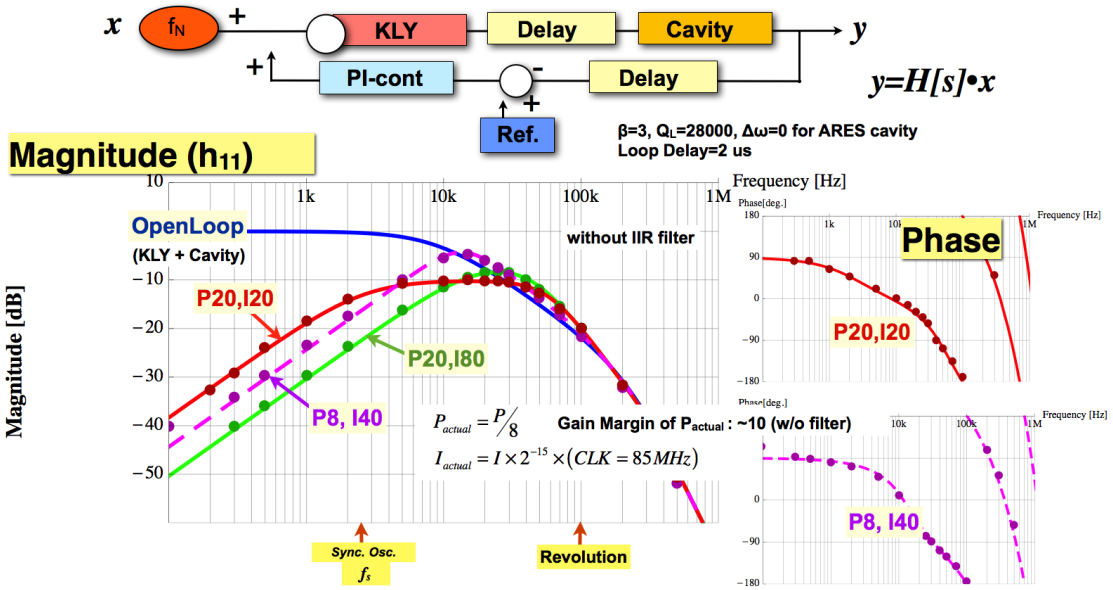

Figure 6.40: Disturbance rejection characteristics inside the closed loop (e.g. driver amplifier noise) for various FB-gains (P: proportional gain, I: integral gain). The solid line indicates the calculation for the tuned cavity, and the circle marks are measured results in a high power test. Response to beam loading has similar property with this plot.

characteristics.

Figure 6.42 shows measured thermal stability of the overall LLRF system before and after the improvement of the BPFs. In the figure, trend histories of monitored amplitude and phase are plotted for two days. The green line indicates the room temperature. The red and blue lines correspond to the cavity-pickup channel (ch 4) and the reference channel (ch 1), respectively. Before the improvement, the stability did not satisfy the requirements. After the improvement, the temperature coefficient of 0.06%/deg. C in amplitude and 0.09 deg. /deg. C in phase was obtained, which satisfy the requirements. Further improvement was also added in the system: by taking the relative phase between the cavity pickup and the reference, that is, the difference between Ch4 and Ch1, then 0.02 deg. /deg. C of phase stability is expected, as shown in the lower right of Fig. 6.42. This can be justified by that both BPFs for ch 4 and ch 1 are housed in a common module case and thus they are affected by similar temperature change.

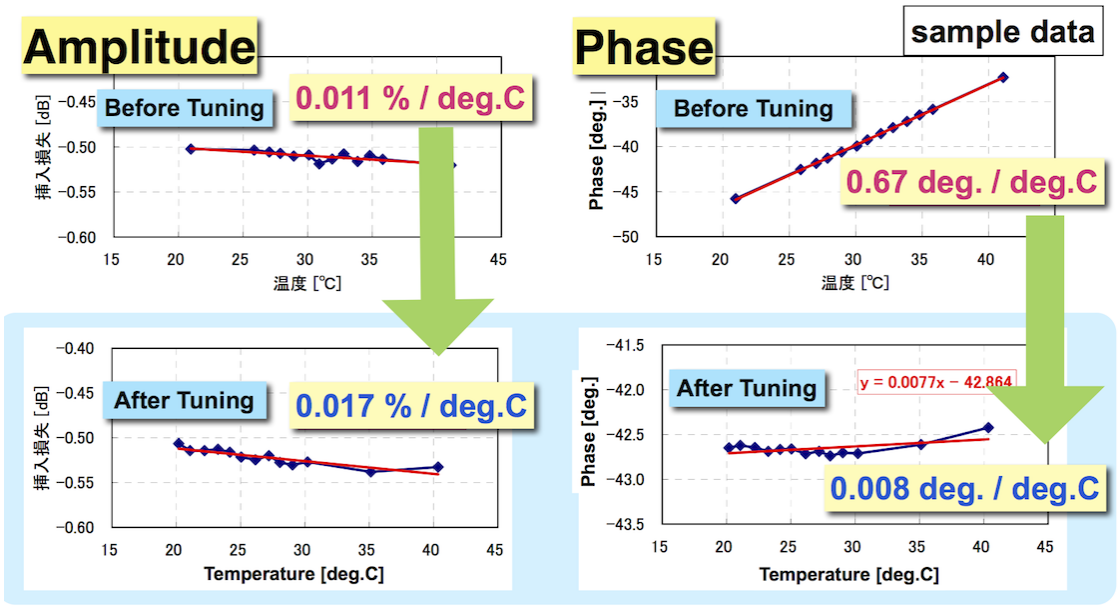

Figure 6.41: Fine-tuning of BPF temperature characteristics was applied for improvement of thermal stability.

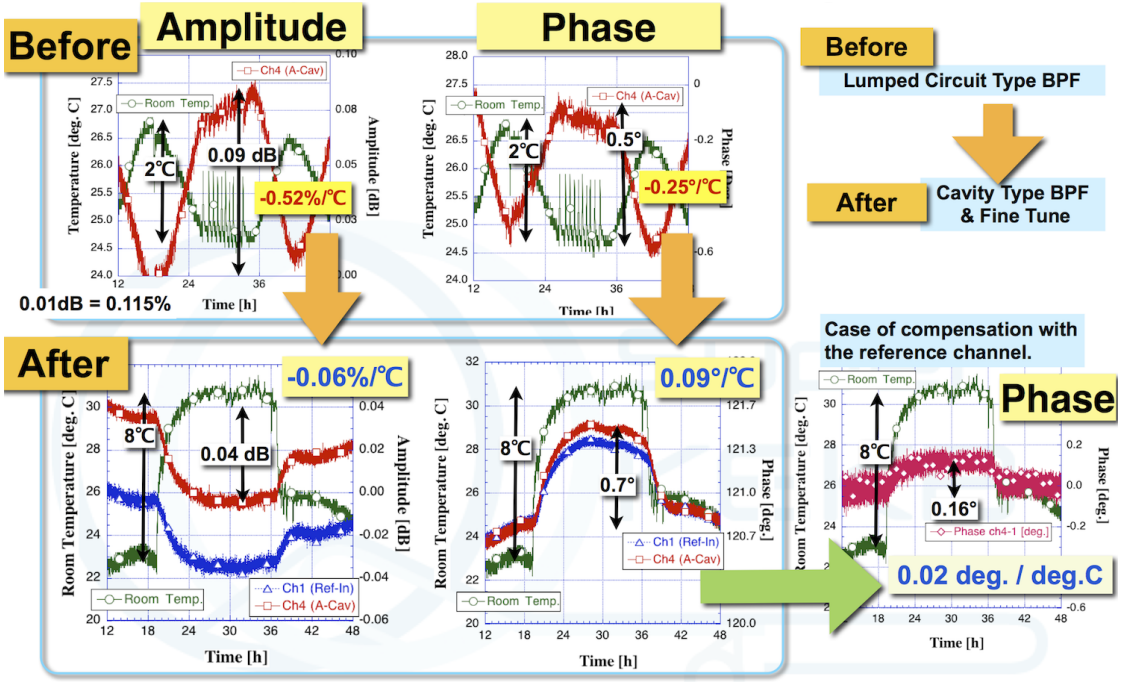

Figure 6.42: Measured thermal stability of the overall LLRF system before and after the BPF-improvement. Trend histories of monitored amplitude and phase are shown.

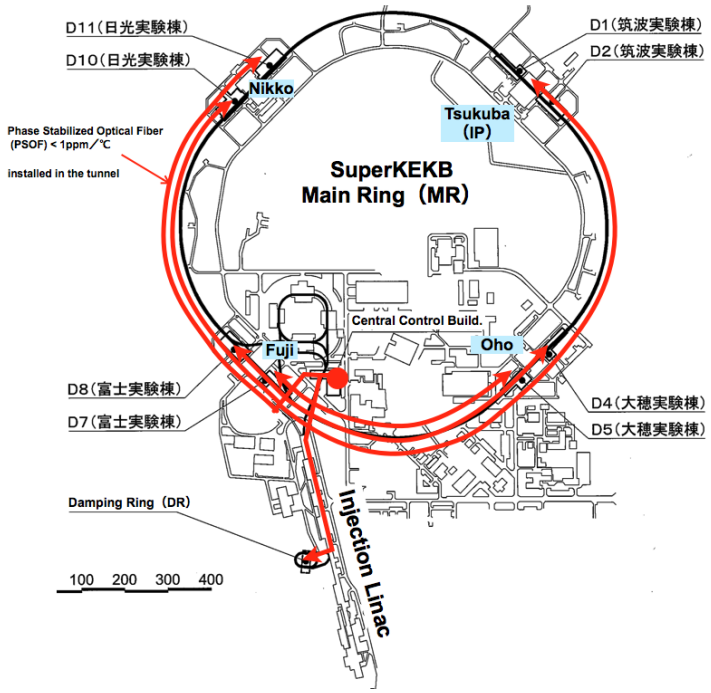

Figure 6.43: Transmission paths of the optical cables installed in the accelerator tunnel for the new RF reference system.

6.4.3 RF Reference Distribution System

For the RF reference of the LLRF control, the required phase stability during beam operation is 0.1 degrees (pk-pk). The RF reference signal of 508.9 MHz is optically distributed from the central control room (CCR) to each RF section, the damping ring, and the Belle-II detector by using "Phase Stabilized Optical Fiber (PSOF)" cables. The PSOF cable has very small temperature coefficient of less than 1 ppm/deg. C (5 ps/km/deg. C). Figure 6.43 shows transmission paths of the optical cables installed in the accelerator tunnel between the stations. They are distributed from the CCR by means of "Star" topology links.

To satisfy the required phase stability, a phase feedback control (or phase lock loop) is needed to compensate for thermal drift of each optical transfer line, even using the PSOF cables. For this we have developed an optical transmitter and receiver system for the thermal drift compensation. A block diagram of this system is shown in Fig. 6.44. The transmitter system is located at the CCR and the receiver systems are located at each control room of the RF section. In the transmitter system, the reference signal of wavelength λ_1 is optically amplified and divided into eight transfer lines. The transferred signal received at each RF section is, after converted to a different

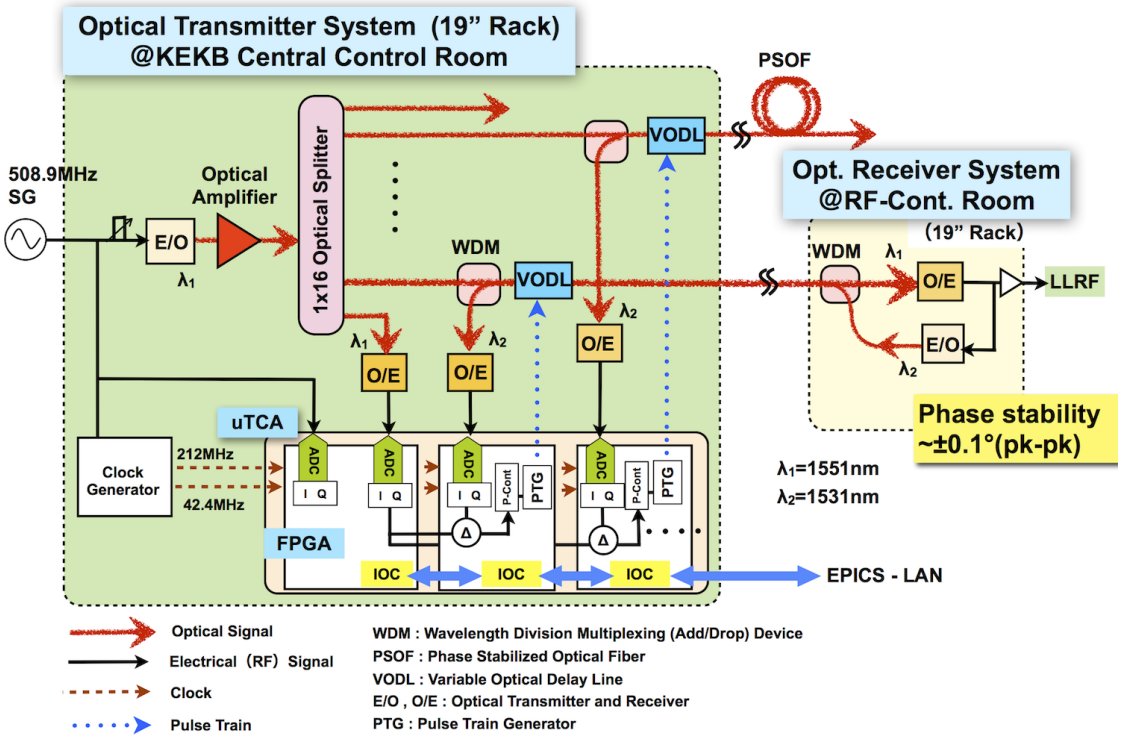

Figure 6.44: Functional block diagram of the RF reference distribution system.

wavelength λ_2 for isolation, returned back passing through the same fiber cable to the CCR by means of Wavelength Division Multiplex (WDM) method. The phase of the return signal is digitally measured by a μTCA-platformed FPGA with direct-sampling method [34] without down-conversion, and then a variable optical delay line (VODL) is controlled to cancel the phase change. Every transfer line has a VODL inserted after the optical divider, and each of them is controlled by the corresponding FPGA individually, as shown in Fig. 6.44. The VODL is a reflection-type optical delay line like a trombone, and it is equipped with a pulse-driven motor, as shown in Fig. 6.45. The FPGA outputs pulse trains to control the VODL to compensate for the phase drift, so that the phases of all RF section are directory locked with a master oscillator at the CCR.

The performance of the phase drift compensation system was evaluated with a measurement setup shown in Fig. 6.46. Phase stability of the transferred signal was measured by using a vector volts meter (VVM) as temperature of the optical cable was changed. A normal optical fiber of the length of 100 m, which has a large thermal coefficient (1.7 deg. /deg. C for 100 m), was used in the transmission. The result is shown in Fig. 6.47: the red line indicates the phase of the transferred signal measured by the VVM, and the dashed blue line is the pulse counts sent to the VODL from the

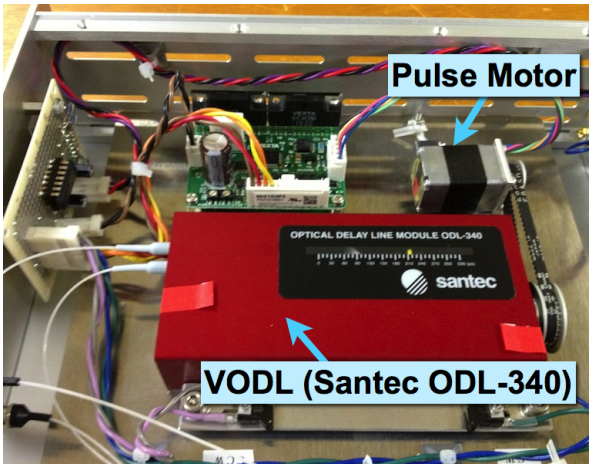

Figure 6.45: Photo of variable optical delay line (Santec Corp., ODL-340), which is additionally equipped with pulse-motor driving mechanism and limit switches.

FPGA. The pulse counts correspond to the phase change of 17 degrees, which is the same value to compensate for the phase change of the cable due to the temperature change. The required phase stability of ± 0.1 degrees was obtained with this drift compensation control system.

The optical transmitter and receiver (E/O and O/E) are the same as those developed for the J-PARC Linac [35], and they have shown long-term reliability during ten-years J-PARC operation. Each of them is equipped with a Pertier device for temperature stabilization. Figure 6.48 shows the phase noise of the optically transmitted signal via the E/O and O/E including an optical amplifier. Sufficiently small phase noise of less than -100 dBc/Hz above 10 Hz was achieved. The noise floor at -140 dBc/Hz due to the E/O and O/E conversion is observed above 10 kHz. This is not a problem, because the frequency range above 10 kHz is out of the bandwidth of the accelerating cavity. The time jitter obtained from the integral of the spectrum from 1 Hz to 10 MHz is 160 fs (rms), which corresponds to the RF phase of 0.03 degrees at 509 MHz. This value includes the time jitter of 80 fs (rms) in the same integral region due to the signal source, Agilent E8663D-UNY, used in this measurement.

6.4.4 CBI Damper

Excitation of longitudinal coupled bunch instabilities (CBI) due to the accelerating mode of RF cavities is a serious concern for a large circumference ring with a high current stored beam. The growth rate of the CBI due to RF cavities can be estimated

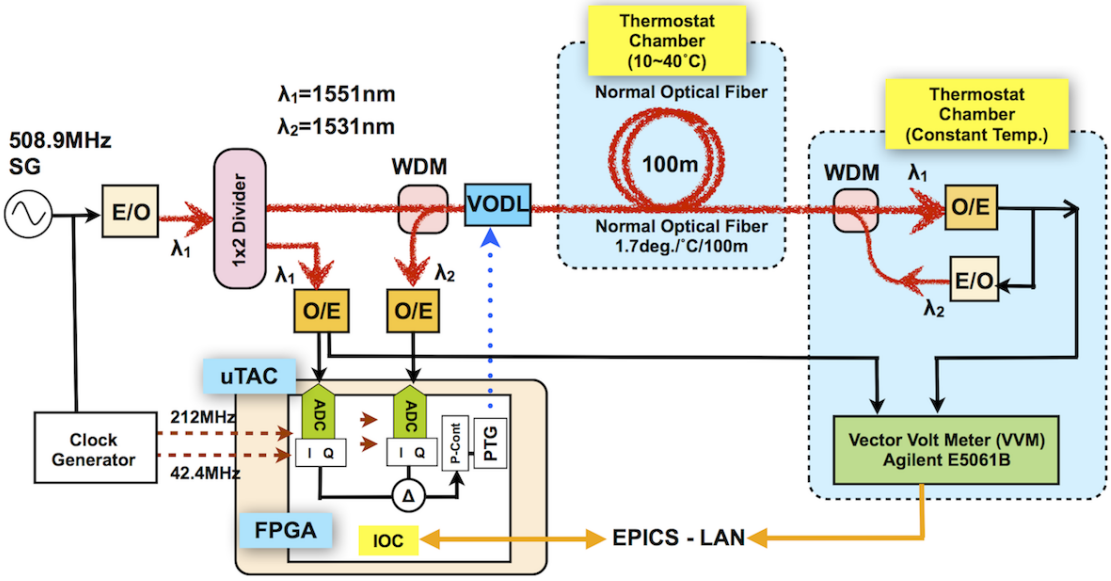

Figure 6.46: Evaluation setup of the VODL control for the temperature drift compensation.

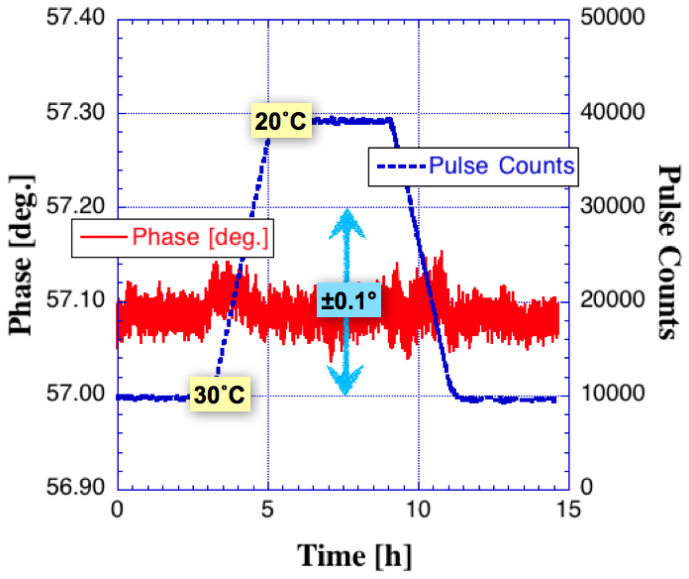

Figure 6.47: Transferred signal phase measured by a vector volt meter (red solid line), and the pulse counts to control the VODL (blue dashed line) in the temperature drift compensation system. Temperature at the cables was changed from 30 to 20 deg. C.

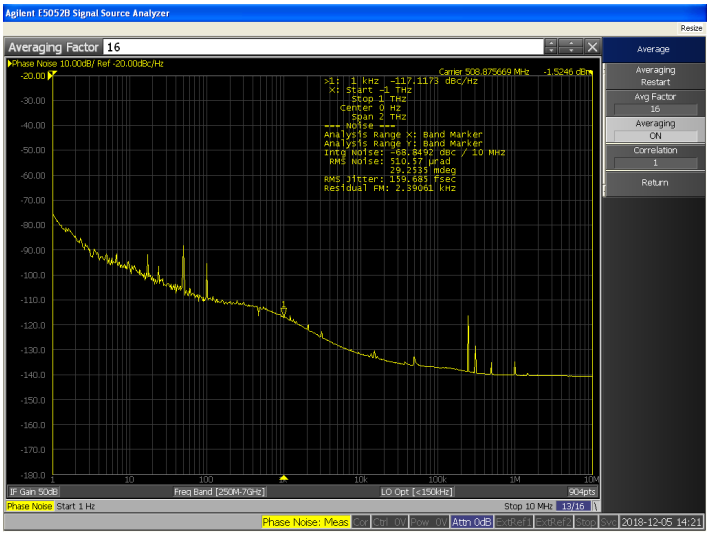

Figure 6.48: Sideband phase noise spectrum of optically-transferred signal (output of the receiver system) in the reference distribution system including a optical amplifier. Noise floor at −140 dB comes from the optical transceiver (E/O and O/E). The time jitter obtained from the integral of the spectrum from 1 Hz to 10 MHz is 160 fs (rms), including the time jitter of 80 fs (rms) due to the signal source.

from the cavity impedance Z_c as

$$\begin{aligned} \tau_\mu^{-1} &= AI_{\rm b}\sum_{p=0}^{\infty}\{\omega_p^{(\mu+)}{\rm Re}Z_c(\omega_p^{(\mu+)}) - \omega_p^{(\mu-)}{\rm Re}Z_c(\omega_p^{(\mu-)})\}, \\ \omega_p^{(\mu+)} &= (ph+\mu)\omega_0 + \omega_s, \\ \omega_p^{(\mu-)} &= \{(p+1)h-\mu\}\omega_0 - \omega_s, \end{aligned} \tag{6.1}$$

where A is a coefficient which depends on the accelerator operation parameters, I_b is the beam current, ω_0 is the revolution angular frequency, ω_s is the angular frequency of the synchrotron oscillation, h is the harmonic number, and μ is the mode number of the CBI. In usual operation with the optimum tuning of the cavities to minimize the input power, the cavities are detuned to the lower side of the RF frequency, $\omega_{rf} = h\omega_0$, to compensate for the reactive component of beam loading. Then the excitation of the $\mu = h-1$ mode (called the $\mu = -1$ mode), $\mu = h-2$ mode ($\mu = -2$ mode), and so on, will be a concern. In the KEKB operation, even with the ARES and SCC cavities, the $\mu = -1$ mode was excited at the beam current of about 1 A. In order to suppress the CBI, a feedback system, so called the $\mu = -1$ damper, was implemented [1, 36]. Fig. 6.49 shows a block diagram of the $\mu = -1$ damping system used in KEKB. It consists of a single sideband pass filter (SSBF) and a digital narrow bandpass filter (DBPF).

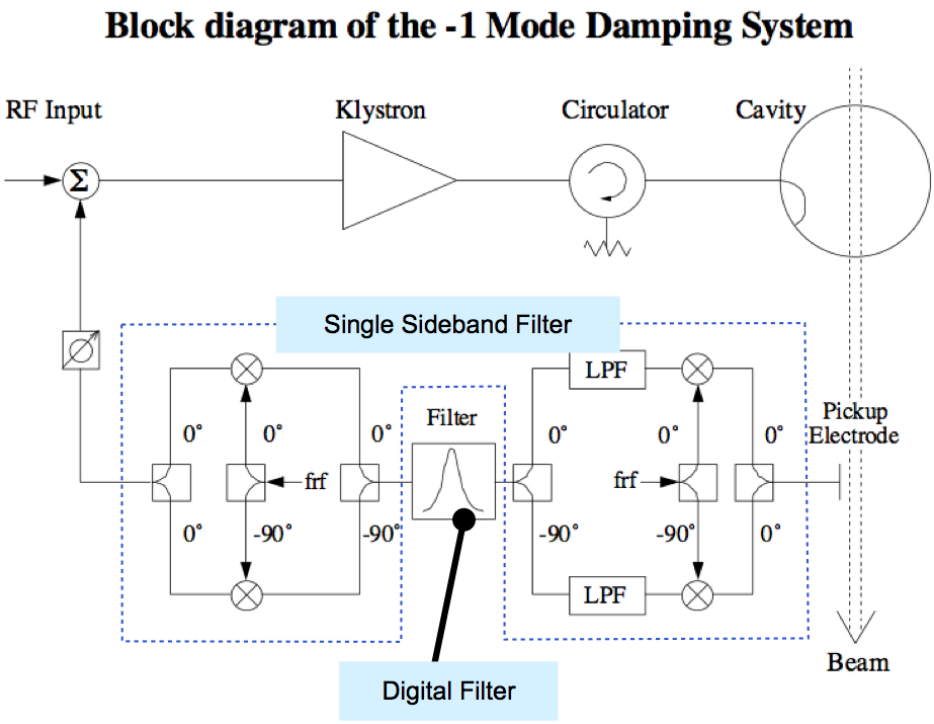

Figure 6.49: Block diagram of the $\mu = -1$ mode damper system used in KEKB operation.

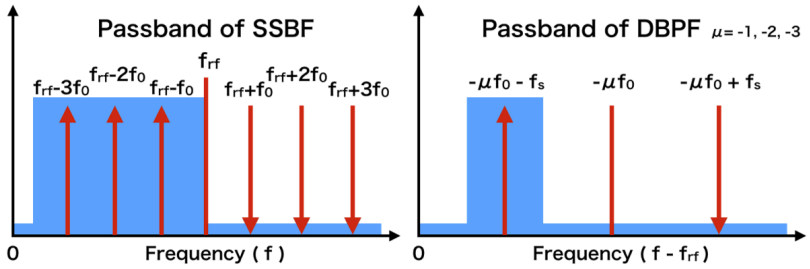

Figure 6.50: Illustration of filtering property of the SSBF (left) and the DBPF (right).

Figure 6.50 illustrates filtering functions of the SSBF (left) and the DBPF (right). The SSBF transmits only the lower sideband of $h\omega_0$ ($= \omega_{rf}$) and rejects the higher sideband: the frequencies contributing to the excitation of CBI, $\omega_p^{(\mu+)}$ in Eq. 6.1, are located in the lower side of ω_{rf} for the modes $\mu = -1$, -2, -3, and so on. The DBPF transmits only the offset-frequency (baseband) of $-\mu\omega_0 - \omega_s$ ($\mu = -1$ for the case of KEKB), which corresponds to the exciting oscillation frequency in the single sideband.

The growth rate of CBI in SuperKEKB is evaluated by Eq. 6.1; the result is shown in Fig. 6.51 for the LER (upper plot) and HER (lower plot) as a function of stored beam current. The solid lines indicate the growth rates in normal operation condition, where all cavities are operated. The growth rate of the $\mu = -1$ mode at the design beam current is much higher than that in KEKB. The dashed lines indicate the growth rates for the case where one cavity is parked at -150 kHz away from the RF frequency due to some trouble in the RF system. In this case, the $\mu = -2$ mode needs to be cured in addition to the $\mu = -1$ mode. Furthermore, in cases when the parked cavity needs to be located at an other frequency, for example at -250 kHz, or when more cavities need to be parked, the $\mu = -3$ mode may also need to be cured. Consequently, a new advanced damper system has been developed for SuperKEKB, which has a higher damping rate as well as capable of curing not only the $\mu = -1$ mode but $\mu = -2$ and -3 modes [37].

A block diagram of the new CBI damper is shown in Fig. 6.52. The DBPF of the new CBI damper is composed of three independent circuits in parallel connection, each adjusted to one of the $\mu = -1$, -2 and -3 modes. The functional block diagram of each circuit of DBPF, implemented in a FPGA, is shown in Fig. 6.53. It has two first-order IIR low-pass filters to make the passband narrower. The center frequency ($-\mu\omega_0 - \omega_s$), the bandwidth, the gain and output phase of the passband can be controlled independently for each mode. The SSBF of the new CBI damper utilizes the I/Q modulator and demodulator of recent commercial products. Measured characteristics of the new SSBF is shown in Fig. 6.54, together with that of KEKB for comparison. The rejection property for the higher frequency side is significantly improved for the new damper by 40 dB, compared to that used in KEKB. The feedback performance of the new CBI damper system was evaluated in a test bench by using a simulant cavity. As shown in Fig. 6.55, the impedance is successfully suppressed at the frequencies corresponding to the excitation of the $\mu = -1$, -2 and -3 modes.

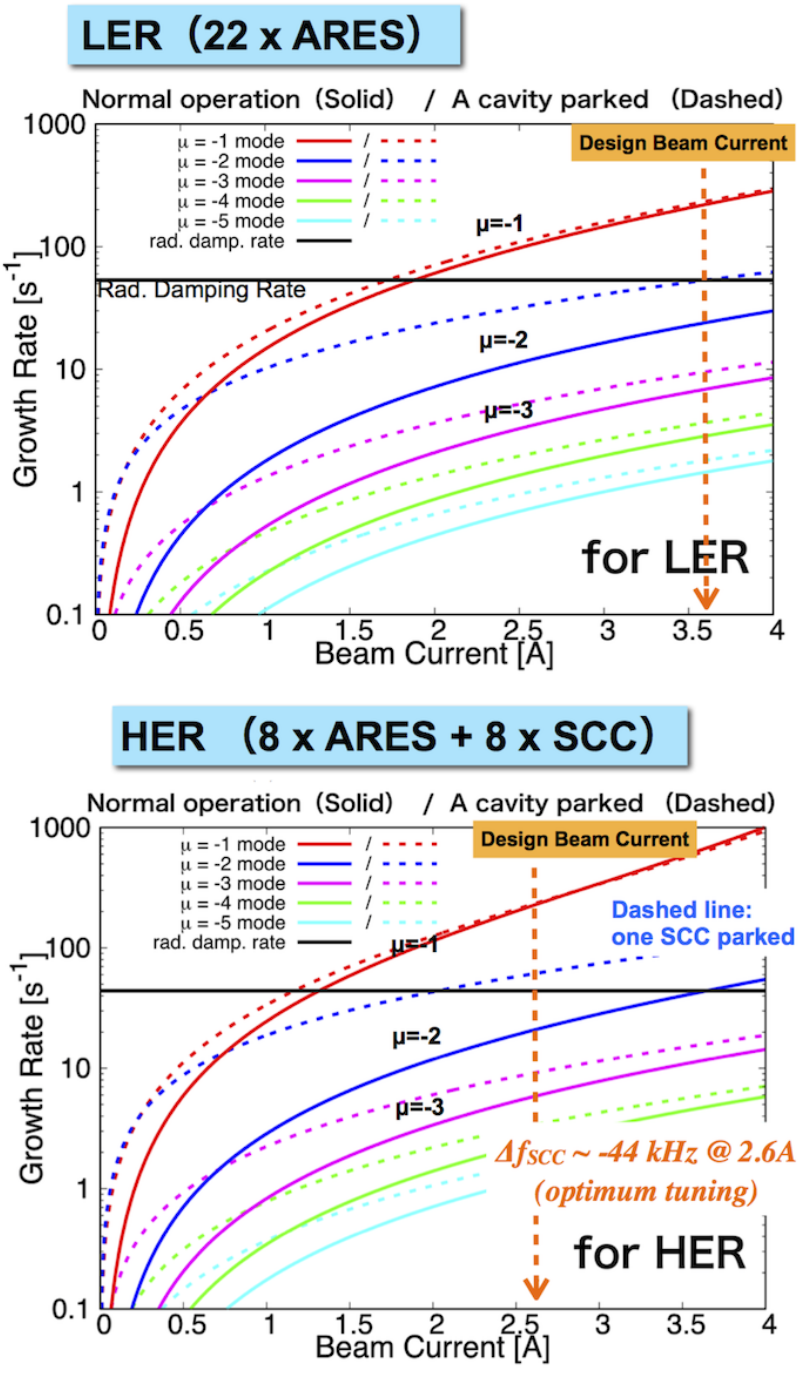

Figure 6.51: Estimated growth rate of CBIs due to the acceleration mode as a function of stored beam current in SuperKEKB. The upper and lower plots are for the LER and HER, respectively. Solid lines indicate the cases for normal operation when all cavities are powered. Dashed lines indicate the cases when one cavity is parked at -150 kHz away from the RF frequency due to some trouble in the RF system.

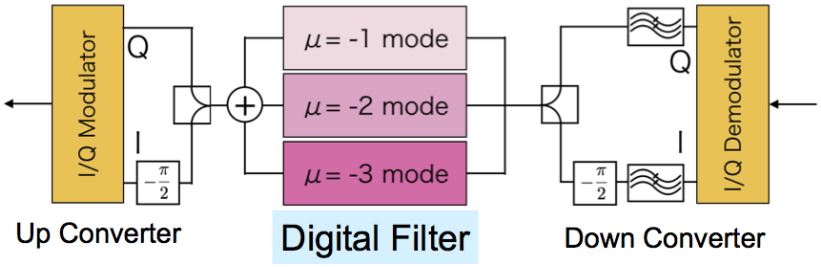

Figure 6.52: Configuration of the new CBI damper for SuperKEKB. The DBPF is composed of three independent circuits in parallel connection, each of which is adjusted to one mode.

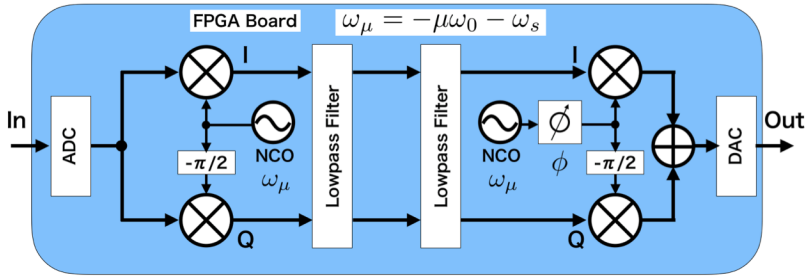

Figure 6.53: The functional block diagram of DBPF, which is implemented in FPGA.

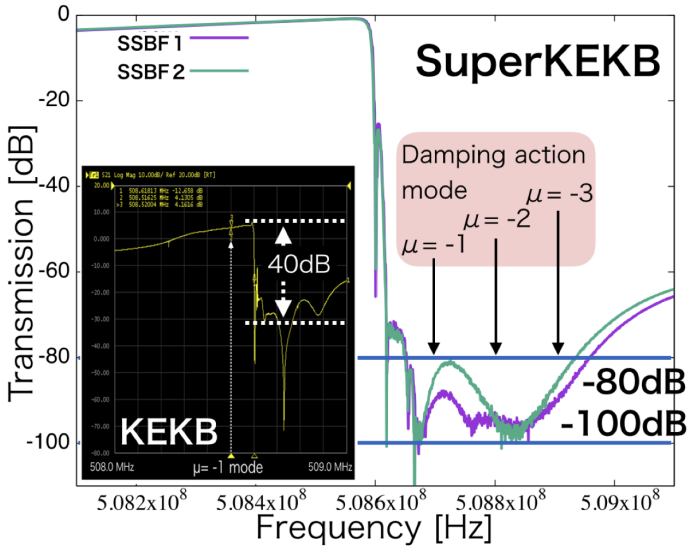

Figure 6.54: Measured characteristics of the new SSBF. The rejection property for the higher frequency side band is significantly improved compared to the damper used in KEKB.

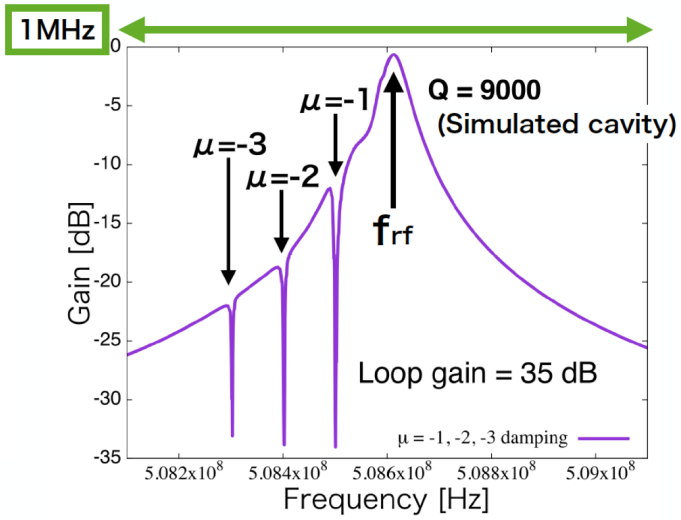

Figure 6.55: Feedback performance of the new CBI damper system evaluated with a simulant cavity. The impedance is successfully suppressed at the frequencies corresponding to the excitation of the $\mu = -1$, -2 and -3 modes.

6.4.5 Bunch Gap Transient

Transient effect caused by an abort gap inserted in a bunch train is a concern for a collider with multi-bunch high current beams. The train gap modulates the amplitude and phase of the accelerating field in the cavities, then the synchronous position changes from bunch to bunch along the train. Relative position shift between the colliding bunches makes a longitudinal displacement of the collision point from bunch to bunch. In the KEKB operation, the phase shift along the bunch train was observed. The measured phase shift along the bunch train agreed well with a simple simulation result for the bunches in most parts of the train. However, a rapid phase change of a few degrees was found at the leading part of the train, which was suspected to be attributed to the excitation of parasitic 0 and π modes of the ARES cavity [38]. No degradation was observed of the luminosity due to the bunch gap transient in the KEKB operation. However, in the SuperKEKB operation, the beam phase difference due to the gap transient will be much larger than that of KEKB due to higher beam currents, even the gap length will be reduced from 5% of the ring in KEKB to 2% in SuperKEKB by improving the rise time of the abort kicker. Furthermore, for the nanobeam collision scheme, where bunches collide at a large crossing angle with a very small β_y^*, this effect may cause some unknown crucial issues to the colliding beams: not only luminosity degradation but even some unknown serious degradation of the beam performance may occur in the worst case.

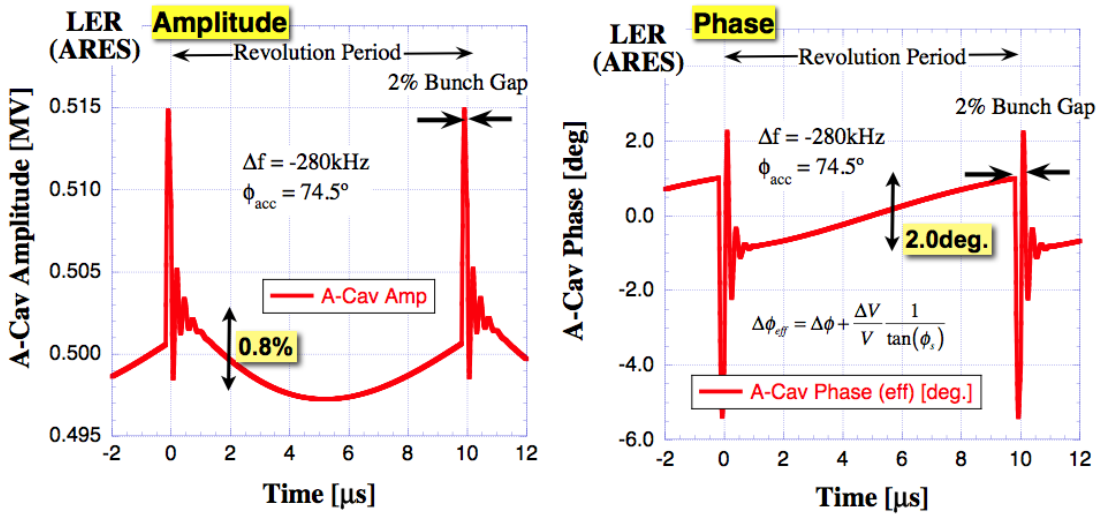

Figure 6.56: Time-domain simulation results of amplitude and phase modulation caused by 2%-bunch gap in LER-ARES cavity. This simulation is including three-cavity structure of ARES.

To evaluate the bunch-gap transient effect for SuperKEKB, we developed a new simulation method [39], which takes into account the parasitic 0 and π modes by treating the three-cavity system of the ARES, instead of an equivalent single cell used in the previous simulation [27]. The gap transient behavior was evaluated using the new simulation with typical operation parameters with the design beam currents of SuperKEKB. Figure 6.56 shows modulation in time-domain of the amplitude and phase of an ARES cavity field in the LER. In the figure, a periodic interval of 10 μs corresponds to the revolution frequency of 100 kHz and the length of the abort gap is 2% of the circumference, ie. $\Delta t_g = 200$ ns. The modulation of the amplitude and phase in the main part of the train except for the leading bunches is approximately 0.8% and 2 degrees, which agrees well with an analytical calculation given by [40]

$$\frac{\Delta V_c}{V_c} = \frac{\omega_{rf}}{2V_c}\left(\frac{R}{Q}\right) I_b \Delta t_g \cdot \tan\phi_{acc}\,, \quad \Delta\phi = \frac{\omega_{rf}}{2V_c}\left(\frac{R}{Q}\right) I_b \Delta t_g\,, \tag{6.2}$$

respectively. In the gap region and at the leading bunches, however, a large phase change of 7 degrees (pk-pk) is seen, as shown in Fig. 6.57, which is a zoomed view of Fig. 6.56 around the gap region. It was confirmed that the large phase change is attributed to the excitation of the parasitic 0 and π modes of an ARES cavity.

Figure 6.58 shows simulation results for the case of the HER, which has two types of cavities: the ARES and SCC. The rapid phase change is also observed for the ARES in the HER, similar as the ARES in the LER. On the other hand, the SCC has no

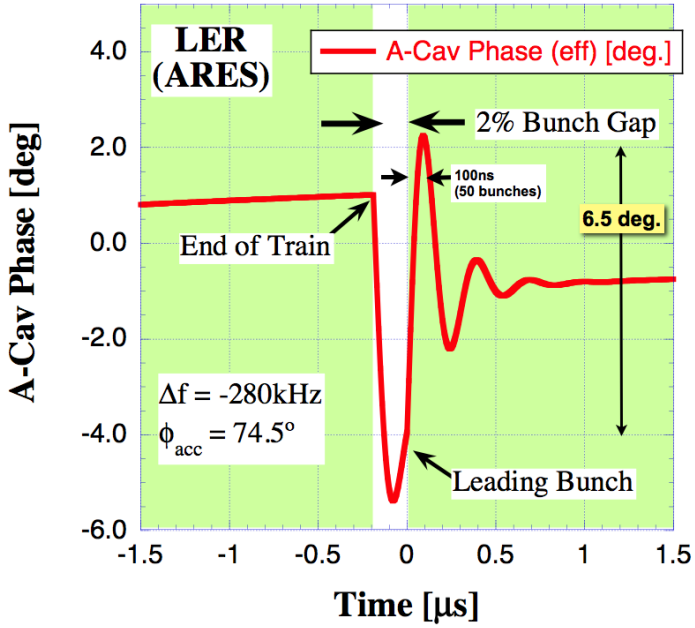

Figure 6.57: Zoomed plot of the phase change shown in Fig. 6.56 at the leading bunches after the bunch gap. The phase of the leading bunches of the train changes approximately 6.5 degrees, which is attributed to the excitation of parasitic 0 and π modes of the ARES cavity.

rapid phase change at the leading bunches, because the SCC's are single-cell cavities. The phase modulation in the most part of the train except for the leading bunches is larger for the SCC compared to the ARES. The vector sum of the field of all SCC and ARES cavities in the HER, which is the field that the HER beam feels in one turn, is shown in Fig. 6.59.

Figure 6.60 (left) shows the phase difference between the LER and HER ($\Delta\phi_{\rm HER} - \Delta\phi_{\rm LER}$), obtained from Fig. 6.56 and 6.59. The red solid line indicates the phase difference between the LER and HER. The phase difference in the most part of the train except for the leading bunches is well less than $\pm$ 1 degree. The relative phase shift at the interaction point (IP) between both beams for these bunches is $\pm(\Delta\phi_{\rm HER} - \Delta\phi_{\rm LER})/4 = \pm(2.5 - 2.0)/4 = \pm 0.125$ degrees, which corresponds to a longitudinal displacement of only 0.04 σ_z for the bunch length σ_z of 5 mm. The right side of Fig. 6.60 shows a zoomed plot around the gap region of the left side of Fig. 6.60. As seen in the figure, at the leading bunches, the phase difference amounts to 5.5 degrees, which may cause some harmful effects for SuperKEKB. As described in Sec. 6.4.2, the gap transient effect can be effectively eliminated neither by the FB nor FF control.

In order to avoid possible harmful effects to the colliding beams, mitigation mea-

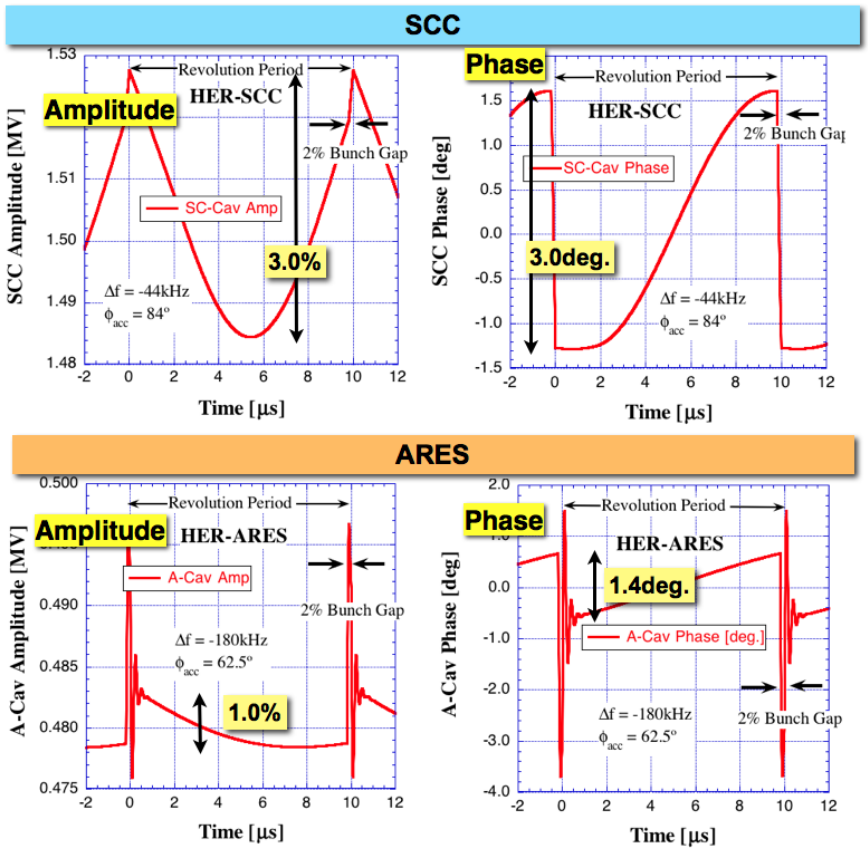

Figure 6.58: Time-domain simulation of phase modulation due to the gap transient for the HER, which has two kinds of cavities: the ARES and SCC.

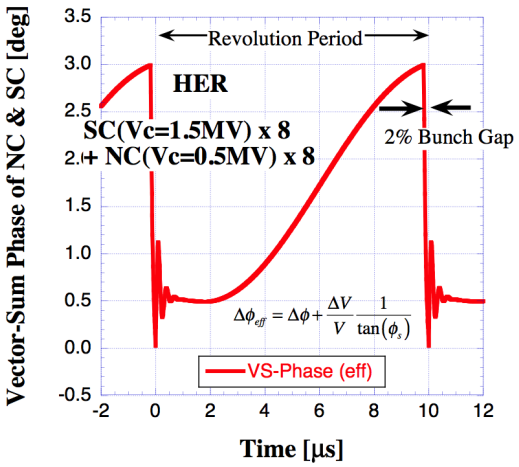

Figure 6.59: Phase modulation of the vector sum of ARES and SCC voltage simulated for HER.

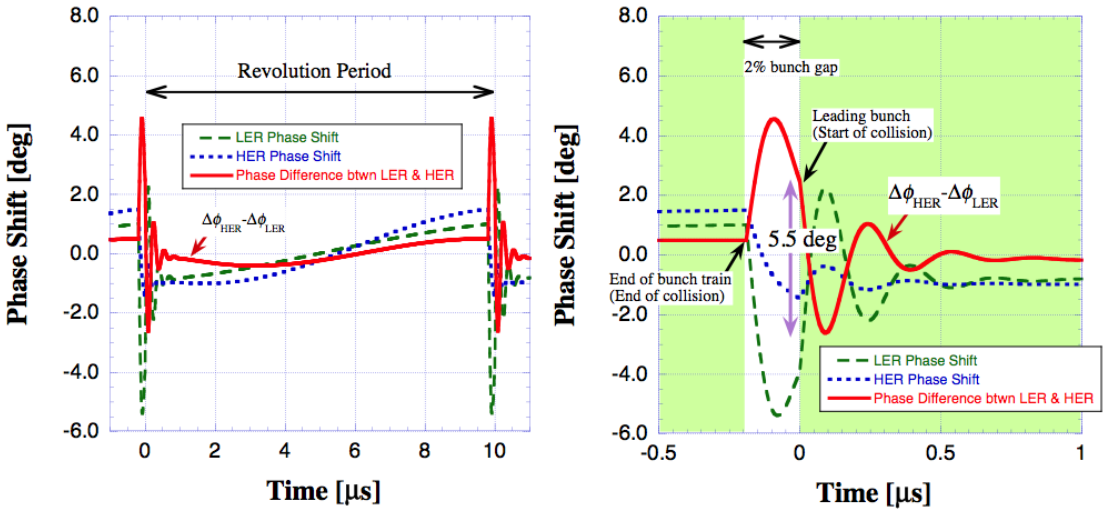

Figure 6.60: Phase difference between the LER and HER; the red solid line indicates $\Delta\phi_{\rm HER} - \Delta\phi_{\rm LER}$. A zoomed plot around the gap region is shown in the right side.

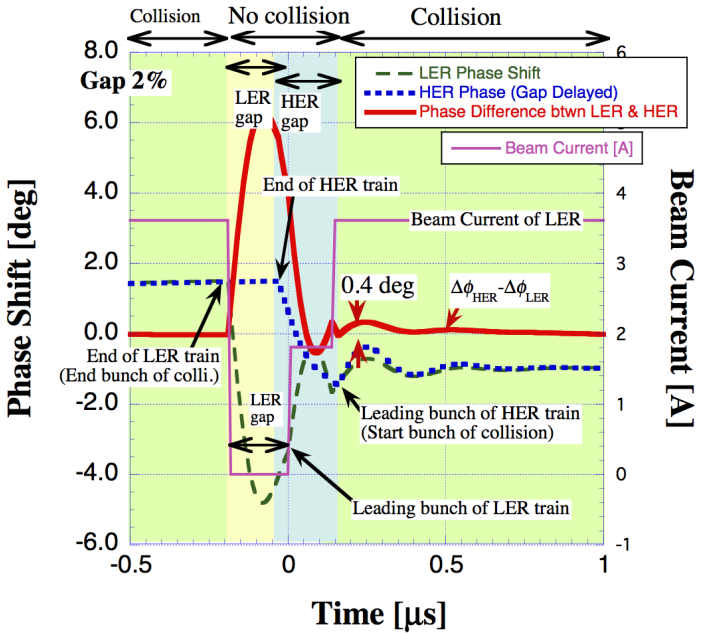

Figure 6.61: An example of the mitigation to avoid possible harmful effects to the colliding bunches due to the gap transient: the gap delay for the HER and filling pattern change for the LER.

Method	Bunch gap	HER delay [ns]	Phase difference $\lvert\Delta\phi_{\rm HER} - \Delta\phi_{\rm LER}\rvert$ [deg.]		Longitudinal displacement @IP	Num. of colliding bunches
			leading	rest		
no cure	2%	0	5.5	0.9	0.44 σ_z	-
HER gap delay	2%	200	2.4	0.9	0.19 σ_z	−2.0%
HER gap delay	3%	300	<0.2	1.6	0.13 σ_z	−4.0%
LER 2 steps + HER gap delay	2%	160	0.4	0.5	0.07 σ_z	−1.6%

Table 6.7: Results of the proposed mitigation measures to reduce the phase difference between the colliding beams.

sures were also investigated. Two mitigation methods were proposed, as shown in Figure 6.61. One method is simply making a delay of the HER gap timing with respect to the LER gap at the cost of a reduced number of colliding bunches. Then the collision is avoided for the leading part of the LER train that has the large rapid phase change. Another method is changing the bunch fill pattern: for example, the LER bunch train is filled up in two steps. Then the phase shift at the leading bunches of the LER is significantly reduced by cancellation of the two step responses of the opposite RF phase. The results with these measures are summarized in Table 6.7. The relative phase difference at the leading part of the colliding bunches is effectively reduced to less than 1 degree. It should be noted that the optimization of the parameters for the mitigation strongly depends on beam operation conditions, which will be investigated during beam operation. For more details of the new simulation and the mitigation results, refer to Ref. [39].

Bibliography

[1] K. Akai, et al., "RF systems for the KEK B-Factory", Nuclear Instruments and Methods in Physics Research A 499 (2003) 45-65

[2] T. Abe, et al., "Performance and operation results of the RF systems at the KEK B-Factory", Prog. Theor. Exp. Phys. 2013 (2013) 03A006.

[3] Y. Yamazaki and T. Kageyama, Particle Accelerators **44**, 107 (1994).

[4] T. Kageyama et al., Proc. PAC97, p. 2902 (1997).

[5] F. Naito et al., Proc. APAC98, p. 776 (1998).

[6] F. Naito et al., Proc. PAC97, p. 2977 (1997).

[7] T. Kageyama et al., Proc. of the 13th Symposium of Accelerator Science and Technology, p. 223 (2001).

[8] T. Kageyama et al., Proc. of the 8^{th} Annual Meeting of Particle Accelerator Society of Japan, p. 1245 (2011).

[9] T. Kageyama, Proc. of 15^{th} Linear Accelerator Meeting in Japan, p. 79 (1990).

[10] T. Kageyama, Proc. of 8^{th} Symp. Accelerator Science and Technology, p. 116 (1991).

[11] Y. Takeuchi et al., Proc. PAC97, p. 2986 (1997).

[12] Y. Takeuchi et al., Proc. of the 4^{th} Annual Meeting of Particle Accelerator Society of Japan and the 32^{nd} Linear Accelerator Meeting in Japan, p. 446 (2007).

[13] Y. Takeuchi et al., Proc. of the 6^{th} Annual Meeting of Particle Accelerator Society of Japan, p. 1093 (2009).

[14] T. Kageyama et al., Proc. of the 14^{th} Symposium on Accelerator Science and Technology, p. 66 (2003).

[15] T. Kageyama et al., Proc. PAC05, p. 1186 (2005).

[16] T. Abe et al., Phys. Rev. ST Accel. Beams **13**, 102001 (2010).

[17] K. Yoshino et al., Proc. of the 7th Annual Meeting of Particle Accelerator Society of Japan, p. 880 (2010).

[18] H. Sakai et al., Proc. PAC05, p. 1294 (2005).

[19] H. Sakai et al., Proc. of the 4th Annual Meeting of Particle Accelerator Society of Japan and the 32nd Linear Accelerator Meeting in Japan, p. 829 (2007).

[20] T. Furuya, et al., "Superconducting Accelerating Cavity for KEK B-factory", Proceedings of SRF1995, CEA-Saclay, France, 1995, p. 729.

[21] T. Furuya, et al., "Operation Status of the KEKB Superconducting Damped Cavity", Proceedings of SRF2001, KEK/JAERI, Tsukuba, 6 - 11 September 2001, p. 599.

[22] T. Tajima, "Development of Higher-Order-Mode (HOM) Absorvers for KEKB Superconducting Cavities", KEK Report 200-10, September 2000, A.

[23] T. Furuya, et al., "Recent Status of the Superconducting Cavities for KEKB", Proceedings of SRF1999, LANL, Santa Fe, NM, USA, 1-5 November 1999.

[24] S. Mitsunobu, et al., "High Power Test of the Input Coupler for KEKB SC Cavity", Proceedings of SRF1995, CEA-Saclay, France, 1995, p. 735.

[25] M. Nishiwaki, et al., "Developments of HOM dampers for SuperKEKB Superconducting Cavity", SRF2013, Paris, September 23-27, 2013.

[26] Y. Morita, et al., "Horizontal High Pressure Water Rinsing for Performance Recovery", SRF2013, Paris, September 23-27, 2013.

[27] K. Akai, et al., "The Low-Level RF System for KEKB", Proc. of EPAC98, pp. 1749-1751 (1998); http://accelconf.web.cern.ch/AccelConf/e98/PAPERS/TUP10G.PDF

[28] T. Kobayashi, et al., "Prototype Performance of Digital LLRF Control System for SuperKEKB", Proc. of IPAC12, pp. 3470-3472 (2012); http://accelconf.web.cern.ch/AccelConf/IPAC2012/papers/thppc079.pdf

[29] J. Odagiri, et al., "Fully Embedded EPICS-Based Control of Low Level RF System for SuperKEKB", Proceedings of IPAC'10, p. 2686 (2010); http://accelconf.web.cern.ch/AccelConf/IPAC10/papers/wepeb003.pdf

[30] ULR: http://ics-web.sns.ornl.gov/css/boy.html

[31] M. Grecki, et al., "Estimation of IQ Vector Components of RF Field - Theory and Implementation", MIXDES 2005, Cracow, Poland, pp. 783-788 (2005).

[32] K. Akai, et al., "Tuning Control and Transient Response of the ARES for KEKB", Proc. of EPAC96, WEP046L (1996);

[33] E. Ezura, et al., "The Low-Level RF System for TRISTAN Main Ring", Proc. of EPAC98, pp. 1660-1662 (1987);

[34] Y. Okada, et al., "Direct Sampling of RF Signal for 1.3GHz Cavity", Proc. of PAC09, pp. 2216-2218 (2009);

[35] T. Kobayashi, et al., "RF Reference Distribution System for J-PARC linac", Nuclear Instruments and Methods in Physics Research A 585 (2008) 12-19

[36] S. Yoshimoto et al., Proc. of 14$^{\text{th}}$ Symp. Accelerator Science and Technology, p. 323 (2003).

[37] K. Hirosawa, et al., "Development of a Longitudinal Feedback System for Coupled Bunch Instabilities Caused by the Accelerating Mode at SuperKEKB", Proc. of IPAC2017, pp. 3989-3991, THPAB115, 2017.

[38] T. Ieiri, at al., "Beam dynamics measurements using a gated beam-position monitor at KEKB", Nuclear Instruments and Methods in Physics Research A 606 (2009) 248-265

[39] T. Kobayashi and K. Akai, "Advanced simulation study on bunch gap transient effect", Phys. Rev. Accel. Beams 19, 062001 (2016)

[40] D.Boussard, "RF Power Requirements for Hight Intensity Proton Collider", Proc. of PAC'91, p.2447 (1991).